2014

Creation and Application of Routines for Determining Physical Properties of Asteroids and Exoplanets from Low Signal-To-Noise Data Sets

Nathaniel Lust
University of Central Florida

CREATION AND APPLICATION OF ROUTINES FOR DETERMINING PHYSICAL PROPERTIES OF ASTEROIDS AND EXOPLANETS FROM LOW SIGNAL-TO-NOISE DATA-SETS

by

NATE B LUST
B.S. University of Central Florida, 2007

A dissertation submitted in partial fulfilment of the requirements
for the degree of Doctor of Philosophy in Physics
in the Department of Physics
in the College of Sciences
at the University of Central Florida
Orlando, Florida

Fall Term
2014

Major Professor: Daniel Britt

ABSTRACT

Astronomy is a data heavy field driven by observations of remote sources reflecting or emitting light. These signals are transient in nature, which makes it very important to fully utilize every observation. This however is often difficult due to the faintness of these observations, often are only slightly above the level of observational noise. We present new or adapted methodologies for dealing with these low signal-to-noise scenarios, along with practical examples including determining exoplanet physical properties, periodicities in asteroids, and the rotational and orbital properties of the multiple asteroid system 2577 Litva.

TABLE OF CONTENTS

LIST OF FIGURES

LIST OF TABLES

CHAPTER 1: INTRODUCTION

Background

Astronomy is unique among the fields of physical science. Most disciplines have the ability to construct and conduct laboratory experiments to test if a hypothesis explains a physical phenomenon. In contrast astronomy almost exclusively relies on passive observations of the subject that is being studied. Many of these observations may be transient with long delays before follow up observations can occur. As such astronomers have great need to make the most out of any observations which are collected, including low signal-to-noise data which may be disregarded in other fields.

There are many types of telescopes used to collect astronomical data, including ground based optical telescopes, radar reflecting telescopes, space based telescopes, and many others. Each of these systems offer a unique view into the heavens, and each come with their own limitations. Ground based scopes are relatively cheap to build (at moderate sizes) and are plentiful providing many opportunities to conduct observations. However, the atmosphere produces challenges that include opacity and light pollution, which are large systematic errors that must be overcome. The atmosphere has less effect on radar observations, however there are only a small number of such facilities, and in the case of solar system observations, they are limited in the targets they can observe by $\frac{1}{r^4}$ falloff in the strength of the radar signal which can be transmitted and detected. There are only a small number of space based telescopes available for a large amount of possible observations. These telescopes are above the atmosphere, and therefore they are unaffected by many systematics that ground based telescopes must contend with. As such, these telescopes are frequently used to conduct observations of phenomenon which no other facility would be able to observe. Theses signals are therefore faint, often at the limit of the hardware to observe, and must contend with systematics near the level of the signal.

For each type of observation, the data collected is similar enough that a common set of analysis tools can make meaningful contributions to characterizing the varying physical phenomenon. We will be presenting new methodologies we have developed or adapted to increase the precision of low signal-to-noise measurements. We make use of these routines to analyze observations of both exoplanets and near Earth objects (NEO), which are two fields of study which low signal-to-noise observations are quite common.

Near Earth Objects

The study and characterization of NEOs is an important topic in the field of planetary science. This research has gained even more prominence in the past few years as it has become an objective of NASAs robotic and human exploration programs, as well as a field which may be opened up to private commercialization in the coming decades. With the recent impact of a small body in Russia, additional interest has been kindled in possible applications for impact mitigation. A major uncertainty for these programs is the diversity and numbers of NEOs along with our relative lack of knowledge of NEOs fundamental physical properties such as density, internal structure, and porosity. These data are necessary for mission design, mission planning, and risk reduction.

Ground based observations of NEOs are a cheap and effective way to characterize the history, evolution, and physical properties of those objects. One particularly simple but useful tool involves measuring the change in brightness of an object over time, its lightcurve. Under normal conditions a small body is approximated, to first order, by a tri-axial ellipsoid. When the object rotates it will present its smaller, then larger sides alternatively. This rotation varies the reflective area of the object, producing a lightcurve whose amplitude varies over time with the changing total reflective area. The rotational period can be determined by observing these variations. Additional amplitude variations can indicate the objects shape as well as major surface features such as craters.

Table 1.1: Table of Binary Periods and densities, a - indicates no data

Body	Period (h)	Density (g/cm^3)	Body	Period (h)	Density(g/cm^3)
2000 CO101	-	-	69230 Hermes	13.892 ± 0.006	-
2006 VV2	-	-	1999 DJ4	17.72 ± 0.01	-
2002 CE26	15.6 ± 0.1	0.9 ± 0.5	2001 SL9	16.4 ± 0.02	$1.8\pm$-
2000 JO23	>360	-	1998 ST49	-	-
2002 XD58	-	-	1999 HF1	14.017 ± 0.004	> 2
1994 AW1	22.3 ± 0.1	-	2001 SN263	149.4 ± 2.28	1.126 ± 0.171
2002 KK8	-	-	2002 AM31	13.35 ± 0.08	-
1999 TO14	1356 ± 12	-	2000 PJ5	14.16 ± 0.04	-
2000 GL74	2034 ± 21	-	1996 FG3	16.135 ± 0.005	1.4 ± 0.3
2006 GY2	11.7 ± 0.4	-	2000 DP107	42.23 ± 0.04	1.7 ± 1.1
1994 CC	200.8 ± 9.6	2.1 ± 0.6	1994 XD	-	-
2003 YT1	36.7 ± 1.8	2.01 ± 0.7	1998 ST27	-	-
2004 DC	23 ± 1	$1.8\pm$-	2004 FG11	20.0 ± 0.4	-
1990 OS	21 ± 3	-	2005 AB	$17.9\pm$-	-
2002 BM26	-	-	2005 NB7	15.28 ± 0.01	-
2000 UG11	18.4 ± 0.2	0.8 ± 0.6	2007 LE	$13\pm$-	-
2007 DT103	15.32 ± 0.1	-	2008 BT18	-	-
2003 SS84	-	-	2008 DG17	-	-
1999 QO	32.25 ± 0.03	-	1139 Atami	$27.45\pm$-	-
2000 AS152	39.21 ± 0.05	-	1727 Mette	20.99 ± 0.02	-
1998 PG	14.0 ± 0.01	-	2044 Wirt	18.97 ± 0.01	-
1862 Apollo	-	-	2577 Litva	35.81 ± 0.01	-
1866 Sisyphus	-	-	3873 Roddy	19.24 ± 0.02	-
3671 Dionysus	27.72 ± 0.02	$1.6 \frac{+0.9}{-0.4}$	1992 AX	13.51 ± 0.0016	-
5143 Heracles	-	-	7369 Gavrilin	49.12 ± 0.02	-
5381 Sekhmet	12.5 ± 0.3	1.98 ± 0.65	8373 Stephengould	34.15 ± 0.10	-
1990 TR	19.47 ± 0.01	-	1987 QD	-	-
7088 Ishtar	20.65 ± 0.02	-	1993 QO	32.25 ± 0.03	-
1991 VH	32.63 ± 0.02	1.6 ± 0.5	2001 OP83	20.76 ± 0.01	-
65803 Didymos	11.9 ± 0.005	1.7 ± 0.4	2000 RY76	62.05 ± 0.05	-
1998 RO1	14.54 ± 0.02	$1.5 \frac{+1.7}{-0.6}$	1999 UT55	14.10 ± 0.01	-
1999 KW4	17.42 ± 0.036	1.97 ± 0.24	1997 CZ5	14.68 ± 0.01	-
2002 RL66	2.492 ± 0.001	-	1993 UC	-	-

In a subset of NEOs additional variations occur regularly but with a different period than the rotation, which indicate the presence of a moon or secondary object (Scheirich & Pravec, 2009). These binary objects provide us with a unique opportunity to measure otherwise unknown physical properties such as system mass and bulk density. However, the pace of binary discovery is well ahead of the follow-up observations necessary to convert them from an astronomical observation on the population of binaries to a geological observation on the structure of NEOs. Of the 66 NEO binaries listed in Table 1.1 below, only 16 have published bulk densities and another 16 do not even have published orbit periods. Furthermore, the error bars on most of the published densities are so large that it is difficult to interpret asteroid structure from these data. Improving the quantity and precision of these can provide fundamental insight into the density, internal structure, and physical properties of NEOs. Improving and extending our knowledge of binary NEO physical properties can provide major inputs into the design and risk reduction of future robotic and human NEO missions.

The secondary periodic signals in binary lightcurves are caused as one or more smaller asteroids orbit about the primary, which is a commonly studied classical dynamics problem. In this arrangement, as the satellite orbits around the primary object there is a possibility that it will pass in front of the primary and block some of its light. This is known as a primary eclipse. Conversely, when the secondary passes behind the object from the observers point of view (a secondary eclipse), some of the flux from the secondary object will be blocked, diminishing the total flux from the system.

With this arrangement it is possible to work out many of the physical properties of these bodies as laid out in (Pravec et al., 1998). The ratio of the effective diameters (an effective diameter is the diameter of a disk required to reflect the observed flux with a given albedo) for the two components of the eclipse can be determined by comparing the flux from the system outside of an eclipse to that of the minimum flux during a total secondary eclipse (when the secondary object is completely

covered by the primary). Once the size ratio has been determined, it can be used in combination with timing information to determine the semi-major axis of the secondary object. As the body passes behind the primary its light will slowly fade until it is blocked completely and after a time interval begin to brighten as it begins to become visable again. Because the relative sizes of the bodies are known, and the period of the orbit can be estimated from the frequency of eclipsing events, the distance the secondary must be from the primary in order for it to spend the given time eclipsed can be determined. The period of the orbit and the distance the body is away from the primary can then be used in Kepler's equations to determine the mass of the primary body. If there are estimates on the volume of the object, the bulk density of the body can be estimated. The density of the object, together with it's spectral type, can be compared with meteorite analogues and estimates of the objects porosity and internal structure can be made (Britt et al., 2002).

Our objective is to maximize the precision and scientific return from NEO lightcurves in order to characterize the rotational properties of these objects. To accomplish this, we have developed centering routines for improving the SNR of our photometry, Bayesian based modeling to robustly analyze uncertainties and fit highly accurate models to low signal-to-noise data, Szego polynomials for approximating frequencies in the data, and wavelet period analysis to see how periodicites are changing in time. The following chapters present how each routine functions and how it might apply to NEO research, and in chapter 5 we present observations and the physical characterization of the NEO 2577 Litva using the outlined methodologies.

Exoplanets

For most of the history of planetary science, the only planetary system available for study was our own solar system. Many elegant theories of planetary formation and evolution were proposed and accepted. These included such ideas as the ”Frost Line” where rocky planets will form inside this line, and gas giants outside where the solar input is low enough that ices can form, and the Nice model (Crida, 2009) of how the giant planets migrated clearing out minor planets from the solar system and created the population distributions we see today. Then in 1995 the first planet orbiting a main sequence star was announced (Mayor & Queloz, 1995). It was an unusual system with a planet weighing several times the mass of Jupiter orbiting closer to its parent star then Mercury to our own Sun. At last however we finally knew for sure what was long suspected, that our solar system was not the only one to contain planets.

Over the next two decades many different telescopes and techniques were used to find additional planets, but the pace of discovery was quite slow. Because these planets are many times fainter then the background signal from their host star very precise, low signal-to-noise, observations must be taken to detect any signal at all. To speed up planet discovery, the Kepler space telescope mission (Borucki et al., 2010) was conceived and subsequently launched in 2009. This telescope was designed to stare at the same small patch of sky, filled with tens of thousands of stars, and monitor for signs of planets.

To search for planets Kepler monitors the brightness of the star over time (its lightcurve). If a planet is present in the system, it will cause the light from the star to dim as the planet passes in front of the star, in what is known as a planetary transit. The telescope has watched the same group of stars for years, looking for these dimming events to happen in a periodic nature. This ensures that transient events, or stellar activity is not mistaken for a planet. As of the writing of this paper there is now a total of 1746 confirmed planets, with 4229 planetary candidates which are awaiting confirmation bringing the total suspected planetary population to 4875 with 452 multi-planet systems as reported by the NASA Exoplanet Archive [1].

As we have mentioned, many of the planetary systems discovered are significantly different from our own. Some of these include large planets in close proximity to their stars (Mayor & Queloz, 1995), others have planets which orbit retrograde with respect to the stars rotation (Narita et al., 2009), and some with seemingly impossible arrangements of planets such that six planets lie within a distance equivalent to the orbit of Venus (Lissauer et al., 2011). These systems challenge our notions of the formation and evolution of solar systems as well as provide a wealth of unique planets to study.

To understand exoplanets and their planetary systems, detailed physical characterization beyond the detection is necessary. These measurements must be done at an even greater sensitivity than the initial detection. The Spitzer space telescope (Werner et al., 2004) is commonly used for this task, as it is above the atmosphere and is set up to monitor the flux from only a few number of stars at a time. Spitzer additionally operates in the infrared portion of the electromagnetic spectrum, which provides a greater contrast between planet and star, as well as providing the ability to make measurements of the composition of planetary atmospheres. These measurements

[1] http://exoplanetarchive.ipac.caltech.edu/

often have signal-to-noise ratios in single digits to low tens. Observations taken with this degree of sensitivity are often very sensitive to the method of data reduction used to perform calibrations, measurements, and modeling. As such more accurate and robust tool-sets lead to finer detail in the measurement physical properties, or the ability to detect properties which otherwise would be undetectable.

Many of the tools we have developed for working with low signal-to-noise lightcurves of NEOs are equally applicable to exoplanet research. In the chapters that follow, we will discuss how these methods can be applied to the area of exoplanet characterizations. This includes methods for maximizing the signal-to-noise during data reduction, and routines for modeling physical properties and their uncertainties. In chapter 4 we present the analysis of several different planetary systems using our methodologies to infer their physical characteristics.

CHAPTER 2: LEAST ASYMMETRY CENTERING METHOD AND COMPARISONS

Introduction

Many analyses in astronomy, such as exoplanet detection, are done on extremely weak signals. With planetary signals being many orders of magnitude weaker than those of the host stars, detecting a primary transit or secondary eclipse often comes down to minimizing the error contribution from the data analysis methods. In aperture photometry the signal is determined by placing an aperture centered on the light source, and summing the pixels, or sub-pixels in the case of interpolation, inside (see Howell, 1989 for a description of methodology and error analysis). Error can be introduced if the aperture is placed incorrectly, missing part of the signal, or including part of the background as signal. This is particularly a problem if the images are under-resolved, as in the many exoplanet light curves obtained by the *Spitzer Space Telescope*. In this chapter we investigate methods to maximize the signal-to-noise ratio (SNR) from aperture photometry by using a variety of high-precision centering methods on these under-resolved, variable-quality datasets.

Working with data collected from the *Spitzer Space Telescope* (Werner et al., 2004), we noted that within the same data set, the standard centering routines, center of light (e.g., Howell, 2006) and fitting a Gaussian, can produce different centers, and thus different model fits (Stevenson et al., 2010). This chapter will compare these two common techniques with a third technique we will introduce, that of finding the point of least asymmetry. We will also determine under what conditions each of these techniques is superior.

Research into determining the center of a stellar image has been ongoing throughout modern astronomy. King (1971) identified the profile of a star versus distance away from its center when using glass plates. This work was later extended by Diego (1985) for array instruments. The authors found that stellar profiles are best represented by a Lorentzian function. We note that while a very accurate mathematical match is required for extracting properties such as area under the curve from a fitted function, it is not as important for determining the center. In cases such as these, any axially symmetric, centrally peaked function should provide comparable results. Due to its simple mathematical form, familiarity, and resemblance to the core of a point spread function, a Gaussian has frequently been used in astronomy.

Mighell et al. (2008) attempt to address some of the same issues by fitting a model PSF to images obtained from the *Spitzer* Infrared Array Camera (IRAC) (Fazio et al., 2004) 3.6 μm bandpass. They show how aperture photometry performed on data can have a strong correlation with the determined (x, y) center position, and they introduce a correction function to deal with this effect. However, we identify that this flux-*vs*.-sub-pixel-position dependency is actually a function of both an intrapixel sensitivity variation, as they suggest, and a pure pixelation effect due to subdividing a continuous distribution function into discrete samples. In this chapter we investigate the direct effect of pixelating a continuous function, as we have robust techniques that take into account both effects (Stevenson et al., 2012a). We find photometry obtained through aperture methods with these corrections is generally superior than that of fitting a function, due to the under-sampled nature of the IRAC camera.

We begin by describing the construction of the datasets used for our tests. This is then followed by a review of fitting a Gaussian and center of light methods for determining the center of a distribution. We introduce a third technique, called least asymmetry, and provide a detailed description of its implementation. We conclude with the centering results from each of the routines on our test data, and a comparison between them.

Synthetic Data and Analysis

The scatter in centering results indicates the precision, but not the accuracy, of a centering technique when used on real data. To assess accuracy (robustness against systematic offsets) we created synthetic datasets with known centers, varying S/N and center location within a pixel.

Synthetic Data

We created three synthetic data sets, one based on the IRAC 8.0 μm channel point response function (PRF),one on the IRAC 3.6 μm channel PRF, and the third on a Gaussian distribution with parameters chosen to approximate the PRF, each oversampled by a factor of one hundred. A PRF is analogous to a PSF, but includes the inherent wavelength-dependent sensitivity of the pixels on the detector as well as the optical distortion. With the PRF we are able to model real observations, while the Gaussian represents a common, if not perfectly justified, approximation to a PSF that is easy to calculate and sufficient for our purposes. It is important to note that the values obtained using these distribution functions are specific only to the functions used. Other distribution functions, which may vary in shape, degree of sampling, or detector response per pixel, will necessarily have different quantitative results. We use these three functions to look at the qualitative differences and performance of each centering routine on idealized and real distribution functions.

We shifted the three oversampled distribution kernels in a 21×21-position grid with shift steps of 5 sub-pixels. This produced 441 different images. The Gaussian kernel was then averaged such that the subpixels fell within original full-pixel boundaries to simulate light falling onto the detector in slightly different locations, while the PRFs were downsampled according to the procedure laid out in the IRAC handbook (IRAC Instrument and Instrument Support Teams, 2013). These frames reflect the PSF in differing pixelation senarios. For each of these binned kernels, we applied

normally distributed noise on a per-pixel basis. In order to determine the per-pixel variance for each Gaussian distribution, we solved the standard charge-coupled device equation (Equation 2.1) for a signal level I, with a given background (bg), detector noise (σ_d), and number of pixels (n_{pix}), such that the per-pixel intensity and additional sources of error when summed satisfy the equation for a given S/N. The units on I and bg are both number of photoelectrons per observation. We make note that in this investigation the background (bg) encompasses all diffuse sources such as zodical light and galactic nebulae. This process was repeated seventy-five times to generate a statistically significant sample size. Finally, we varied the S/N to investigate the effect that different observing conditions may have on centering.

$$\frac{S}{N} = \frac{I}{\sqrt{I + n_{pix}(bg + \sigma_d^2)}}. \tag{2.1}$$

Altogether we had three data sets, Gaussian and two PRFs, with 19 S/Ns, each with 441 sub-pixel locations containing 75 frames with separately drawn random noise, for a total of 1,256,850 samples.

Methods and Analysis

In aperture photometry, we wish to maximize the number of photons that come from the body of interest, while minimizing those contributed by the background. This normally involves considering all flux within a certain region to be flux from the object. This leads to the issue of determining the center of the region of interest from the finite sampling provided by detector pixels. Below we discuss three methods, all of which solve this problem, but differently.

Center of Light

Determining the center of a distribution using the center-of-light method is computationally and conceptually straightforward. The functional form is the same as that for center of mass,

$$X = \frac{\Sigma_i m_i x_i}{\Sigma_j m_j}, Y = \frac{\Sigma_i m_i y_i}{\Sigma_j m_j}, \tag{2.2}$$

where m_i is the "mass" or weight at each point, and y_i, and x_i are the distances of the points away from the origin in the y and x directions, respectively. This performs an average in each dimension weighted by the amount of "mass" present at each location, resulting in the center location about which the mass is distributed. In this case, however, the "mass" at each point is the flux contained in a given pixel. This method is also commonly known as centroiding. However, a center-of-mass calculation is only equivalent to a geometric centroid when the object has constant density, such as determining the center for an irregularly shaped but uniformly dense block. Since this is not the case for a stellar image, as the amount of mass (light) per unit volume (pixel) is not constant, we avoid the term in this paper.

The major advantage to this centering routine is that it assumes no inherent distribution of the light. As a result, it works for irregular shapes; however, this is also its weakness. By assuming nothing about the object's shape, the routine is very sensitive to outliers in the distribution of additive noise within the image. Where a nearby warm pixel might not seriously affect a Gaussian fit, it would weight the center-of-light away from the true center.

Gaussian Centering

Assuming that the PRF combined with noise is axially symmetric, it is possible to derive sensible centers by modeling it with a two-dimensional (2D) Gaussian,

$$G = Ae^{-\frac{1}{2}(\frac{(x-\mu_x)^2}{\sigma_x^2}+\frac{(y-\mu_y)^2}{\sigma_y^2})}, \tag{2.3}$$

where A is a scaling constant, x and y are the position of a pixel, μ_x and μ_y are the true positions of the source in x and y, and the variances in x and y are given by σ_x^2, σ_y^2. Because the center is found by fitting an analytic function, this routine is fairly robust against low variations, or a small number of larger variations, due to noise. However, by assuming the distribution function is symmetric, this routine will produce inaccurate centers when the distribution is asymmetric. This deviation may arise from insufficient signal, asymmetric pixelation, speckles, or an inherently asymmetric PRF.

Least Asymmetry

Least asymmetry was originally devised by James Gunn (Princeton University) for use in radio astronomy. Russell Owen (University of Washington) then used it in a software package[1] to drive the pointing of telescopes, but did not explore it much further. In personal communications with Owen, he shared the methods, background, and algorithm with us. A non-exhaustive search through the literature did not produce references, so we present the full algorithm here with examples.

Up to this point, we have discussed determining centers using a weighted average and minimizing a functional model. Least asymmetry accomplishes centering by first performing a transformation on the data to produce a new space with different properties, similar in idea to a 2D cross correlation.

[1] http://www.astro.washington.edu/users/rowen/PyGuide/Manual.html

We begin with an asymmetric distribution that is a result of the optical aberrations in the system as well as the presence of noise in the measured signal. Figure 2.1 depicts such an asymmetric signal. We propose that the center is the point about which the distribution is most symmetric. We define the asymmetry of the signal as a function of position as

$$A(x,y) = \sum_{0}^{R} Var(\Phi(r)) * N(r), \tag{2.4}$$

where the discrete index r indicates the particular radial bin, Var is the variance operator, Φ is the flux, and $N(r)$ gives the number of pixels at a given radius for weighting. Equation 2.4 remaps images to a space in which the intensity is more normally and symmetrically distributed, as demonstrated by fitting a Gaussian to the image in asymmetry space *vs* flux space. In principle, if this were a continuous dataset, we could continue this process until the point of minimum asymmetry was absolutely determined. Because datasets collected using imaging arrays are discretely sampled, we take advantage of the increased symmetry and use established centering routines to determine the point of minimum asymmetry to sub-pixel accuracy.

To determine the point of minimum asymmetry, we calculate the value of asymmetry about each pixel in the shaded region in Figure 2.1. The calculation begins by laying an aperture about a given pixel as indicated in Figure 2.2. This region, which we note extends outside the window undergoing transformation, is used to create a radial profile, (see Figure 2.3), with discrete radii corresponding to the pixel centers, as shown in Figure 2.4. The radial profile for the particular pixel shown in Figure 2.2 is given in Figure 2.5. Because we only choose radii corresponding to pixel centers, the radial bins are groupings of points at discrete distances. As a general example of asymmetry, Figure 2.3 shows profiles corresponding to low (top) and high (bottom) asymmetry.

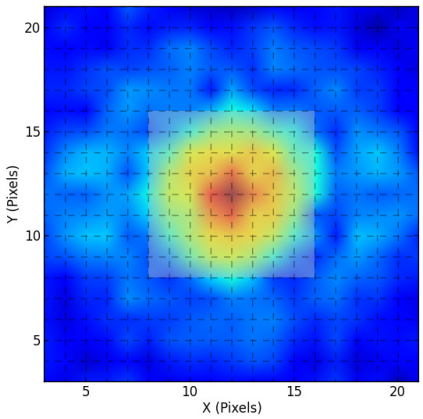

Figure 2.1: Asymmetric image for which the center is to be determined. The asymmetry value will be calculated for each pixel in the shaded region near the center of the image.

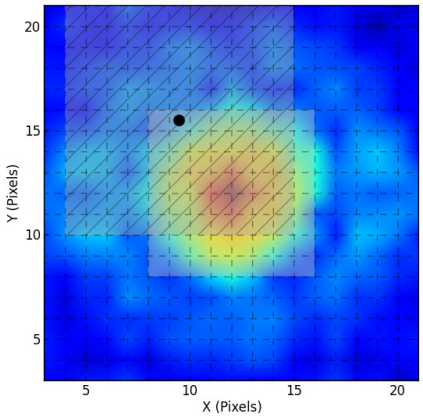

Figure 2.2: Asymmetric image with thatched region to indicate the region of transform for the dotted pixel

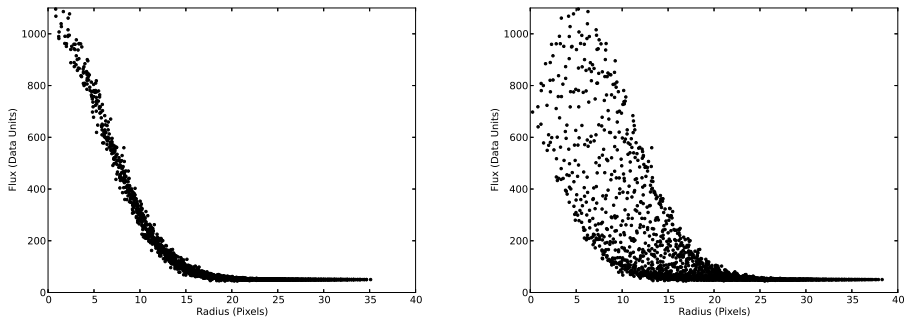

Figure 2.3: Stellar radial profiles. Left: When the profile is centered on the star, the variance in each radial bin is small, indicating low asymmetry. Right: When the profile is centered five pixels from the stellar center, the variance in each bin is high because the light is asymmetrically distributed about this point. The least asymmetry method works by minimizing the sum of the variances in all of the radial bins.

The generated radial profile is used in conjunction with Equation 2.4, to calculate the value of asymmetry. We repeat this process for each pixel in the conversion window to produce the asymmetry values depicted in Figure 2.6. Finally, we use a traditional centering method in asymmetry space to determine the center with sub-pixel accuracy. In our cursory tests, we determined Gaussian centering performed better than center of light.

It is improper to do photometry on Figure 2.6 as the values correspond to sums of variances and not flux values. The figure does not represent a cleaned up image but is merely an array representation of the distribution of asymmetry values of the original image. The center as determined from this distribution must be used in flux space to determine photometric measurements.

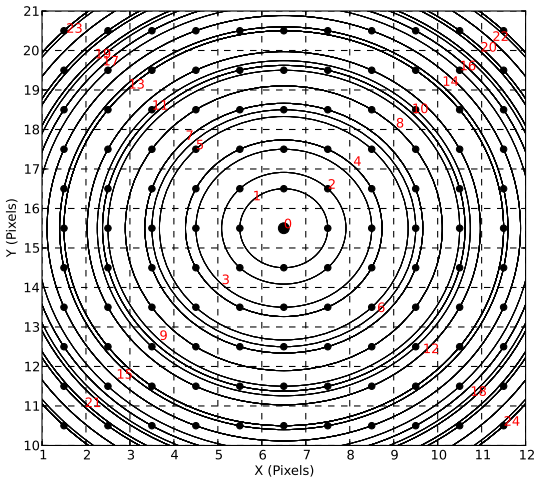

Figure 2.4: Radii used to generate radial profile in the region of transformation.

Results

We applied the three methods to our three synthetic datasets to determine which performed the best under different circumstances. Although specific values differed between the two PRFs, qualitatively the results are similar. As we are more concerned with the qualitative results of the centering routines we will present only the 8 µm bandpass results in this section for comparison. Similar figures for 3.6 µm bandpass are available in Appendix A.

To test the precision and accuracy of these routines, we ran each method against the synthetic data described in Section 2 to produce calculated x and y values for each frame, a total of over 3.6 million centering calculations. To compare results we create images, see Figure 2.7, in which the axes correspond to the sub-pixel location and the values correspond to the figure of merit: the mean distances of the position residuals.

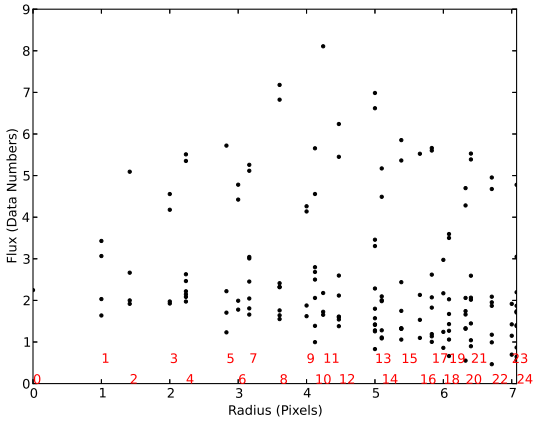

Figure 2.5: Radial profile corresponding to our region of transformation. Red numbers correspond to the labels of radii shown in Figure 2.4

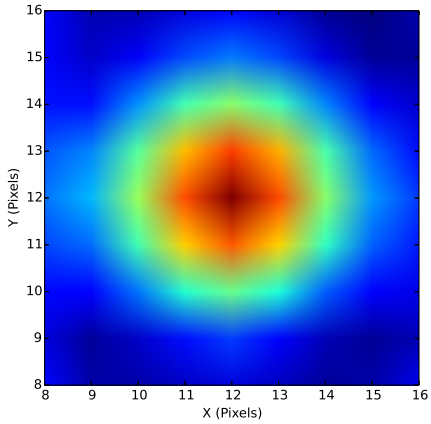

Figure 2.6: Image of asymmetry space for the region converted from Figure 2.1.

Tables 2.1 and 2.2 summarize these data. The values presented are the average over all subpixel locations, indicating the total expected error. The value in parenthesis next to the mean is the standard deviation over each of the trials used to construct the mean. These can be thought of the error in the error, or the precision with which the resulting mean offset can be expected. The optimum method at each S/N is shaded gray.

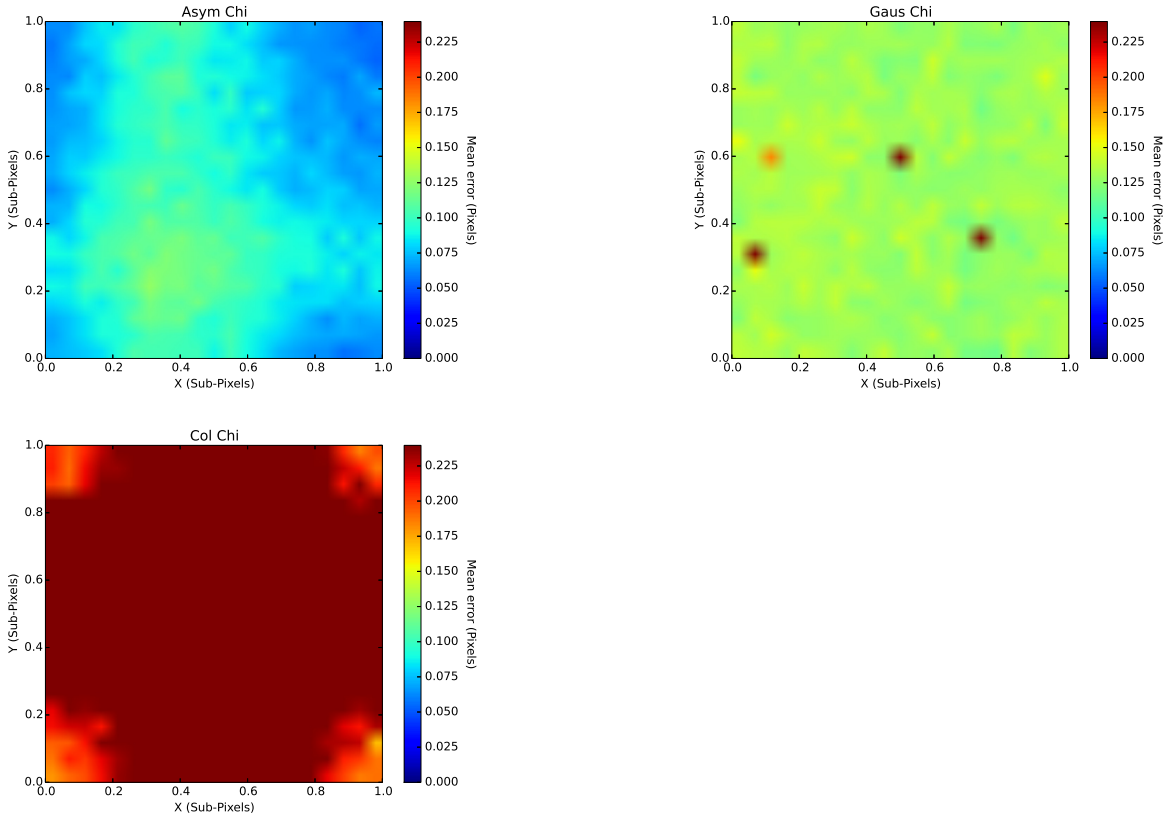

Figure 2.7: Centering quality in sub-pixel space for least asymmetry (top), Gaussian (center), and center of light (bottom) for the 8 μm bandpass PRF at S/N 10. Blue represents better centering, red worse. The cross pattern arises from a combination of a pixelation effect and the non-uniformity of the PRF.

Table 2.1 gives the results for centering the Gaussian kernel. Least asymmetry performs the best in the noisiest conditions, and Gaussian centering performs best at high S/N. This is expected given that the distribution is constructed from a Gaussian kernel. At low S/N, Gaussian fitting and center of light are more easily thrown off. In the case of least asymmetry, however, the transformation converts to a space that is more normal, so the signal in the asymmetry space is stronger. As the signal continues to increase in strength, fitting a Gaussian becomes more accurate at a rate faster than that of asymmetry. Center of light not only performs the worst in all cases, but its accuracy improves at a much slower rate than that of the other two routines.

The deviation of the *Spitzer* 8 μm bandpass PRF from normal is evident in Table 2.2. For the lowest-S/N scenarios the distribution deviates furthest from normal and fitting a Gaussian in flux or asymmetry space is out-performed by center of light, though the centering still has large errors. Once the signal is discernible over the background, asymmetry is the preferred choice for all of the test cases. Each of the routines tested all show improvement with increased S/N, as would be expected, each converging at different rates in both precession and accuracy.

Gaussian centering is noticeably lacking throughout Table 2.2 because the asymmetric light distribution skews the Gaussian centering consistently away from the correct answer. The Gaussian centering routine was very precise, but not accurate, giving it a larger sum of squared residuals. This effect is illustrated in Figure 2.8, where the residuals of Gaussian centering are more tightly packed than the residuals from asymmetry. If it could be accurately explored for a given distribution of light at particular gains and S/Ns, it might be possible to develop corrections to be used with Gaussian centering to make it more accurate. These corrections would, however, only be good for the particular PRF, S/N, and sub-pixel location. In the lowest-S/N cases, least asymmetry proves to be both more precise and more accurate than Gaussian centering.

Conclusions and Future Work

Tables 2.1 and 2.2 show which centering methods perform better under particular circumstances and are not intended as a comprehensive guide for which centering method is the best. A different PRF will necessarily have different results, such as can be seen in Appendix A.

Table 2.1: Gaussian Kernel Mean Positional Error (Pixels)

S/N	Asymmetry	Gaussian	Center of Light
1.0	0.4407 (0.0515)	20.619 (23.316)	0.7803 (0.2691)
2.0	0.1247 (0.0120)	0.5396 (0.4997)	0.7601 (0.2622)
3.0	0.0845 (0.0084)	0.1380 (0.2106)	0.7408 (0.2555)
4.0	0.0682 (0.0072)	0.0778 (0.0590)	0.7223 (0.2491)
5.0	0.0594 (0.0069)	0.0598 (0.0367)	0.7060 (0.2459)
6.0	0.0538 (0.0068)	0.0481 (0.0236)	0.6890 (0.2399)
7.0	0.0500 (0.0069)	0.0406 (0.0072)	0.6727 (0.2343)
8.0	0.0473 (0.0071)	0.0373 (0.0072)	0.6570 (0.2288)
9.0	0.0452 (0.0073)	0.0356 (0.0101)	0.6415 (0.2225)
10.0	0.0436 (0.0073)	0.0336 (0.0114)	0.6284 (0.2170)
20.0	0.0374 (0.0087)	0.0225 (0.0069)	0.5096 (0.1759)
30.0	0.0357 (0.0094)	0.0178 (0.0066)	0.4242 (0.1464)
40.0	0.0349 (0.0098)	0.0150 (0.0032)	0.3600 (0.1242)
50.0	0.0346 (0.0100)	0.0141 (0.0134)	0.3100 (0.1069)
60.0	0.0343 (0.0102)	0.0122 (0.0109)	0.2702 (0.0932)
70.0	0.0341 (0.0103)	0.0114 (0.0108)	0.2379 (0.0820)
80.0	0.0340 (0.0104)	0.0103 (0.0066)	0.2111 (0.0727)
90.0	0.0339 (0.0105)	0.0102 (0.0129)	0.1883 (0.0655)
100.0	0.0338 (0.0106)	0.0108 (0.0244)	0.1693 (0.0589)

Table 2.2: 8 μm PRF Kernel Mean Positional Error (Pixels)

S/N	Asymmetry	Gaussian	Center of Light
1.0	0.8081 (0.0635)	89.66 (131.467)	0.4457 (0.1172)
2.0	0.4829 (0.0435)	0.8983 (3.5599)	0.4343 (0.1141)
3.0	0.2332 (0.0216)	0.2195 (0.1328)	0.4233 (0.1110)
4.0	0.1637 (0.0149)	0.1714 (0.0649)	0.4128 (0.1081)
5.0	0.1332 (0.0135)	0.1556 (0.0443)	0.4028 (0.1053)
6.0	0.1158 (0.0134)	0.1479 (0.0419)	0.3932 (0.1026)
7.0	0.1047 (0.0138)	0.1427 (0.0342)	0.3840 (0.1001)
8.0	0.0970 (0.0144)	0.1373 (0.0303)	0.3751 (0.0976)
9.0	0.0916 (0.0151)	0.1343 (0.0175)	0.3681 (0.0961)
10.0	0.0876 (0.0158)	0.1305 (0.0070)	0.3597 (0.0936)
20.0	0.0722 (0.0196)	0.1253 (0.0038)	0.2925 (0.0752)
30.0	0.0685 (0.0212)	0.1245 (0.0036)	0.2442 (0.0620)
40.0	0.0670 (0.0219)	0.1242 (0.0035)	0.2080 (0.0523)
50.0	0.0662 (0.0224)	0.1240 (0.0034)	0.1799 (0.0449)
60.0	0.0657 (0.0226)	0.1238 (0.0033)	0.1577 (0.0392)
70.0	0.0654 (0.0228)	0.1238 (0.0033)	0.1396 (0.0347)
80.0	0.0651 (0.0229)	0.1237 (0.0032)	0.1247 (0.0310)
90.0	0.0649 (0.0231)	0.1236 (0.0032)	0.1123 (0.0281)
100.0	0.0648 (0.0231)	0.1236 (0.0032)	0.1019 (0.0258)

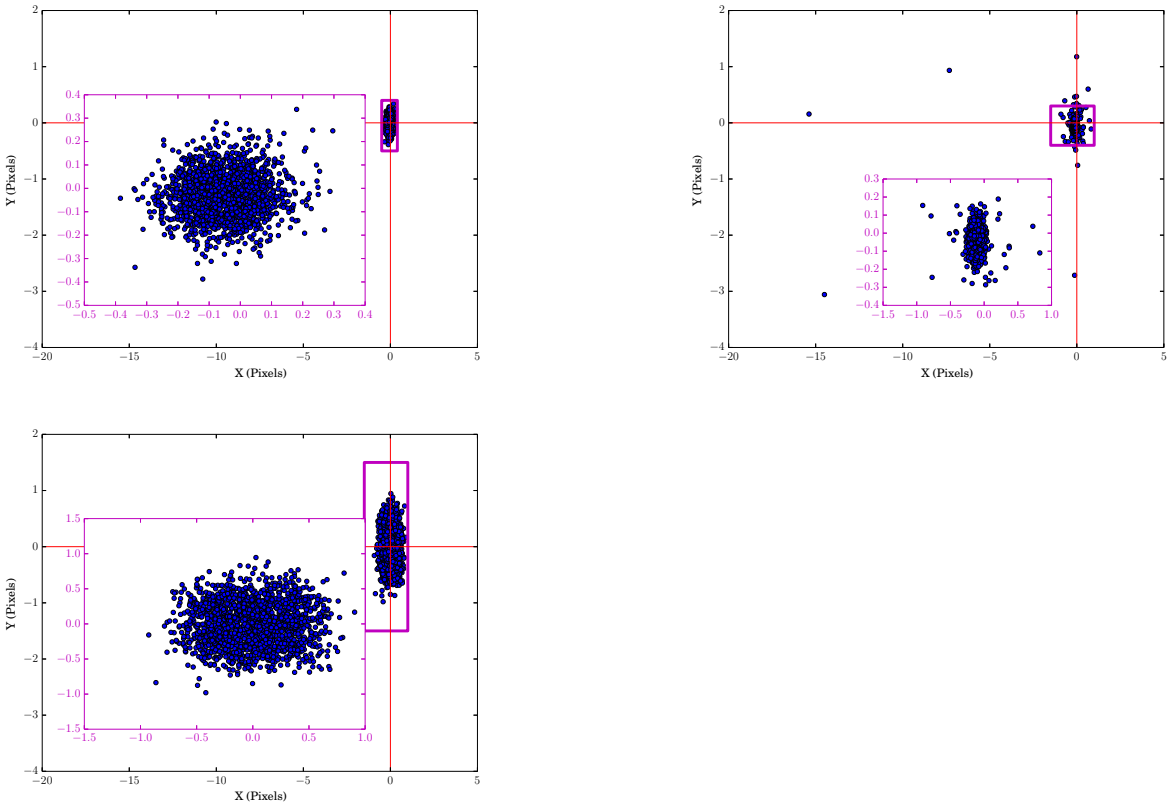

Figure 2.8: Routine precision at S/N = 5 on the 8 µm PRF. Top: The residuals from least asymmetry centering. Middle: The residuals from Gaussian centering. Bottom: The residuals from Center-of-Light centering. Asymmetry performs best at low S/N. Note the axes are the same scale, but the subfigures are a larger view of the magenta square and differ in scale to provide further detail. The red lines indicate the zero point.

However, these tables are useful for gaining a general understanding of these centering routines. First, we note that centering with asymmetry performs well under a variety of conditions and is just as viable as the other two centering choices. For example, least asymmetry outperforms center of light by about a factor of seven at a S/N of 10. Second, under high noise conditions, fitting the analytic function of a Gaussian gives an ill-defined minimum in parameter space and thus poor centering. Finally, center of light outperforms the other two routines in the lowest S/N for the *Spitzer* PRF distribution as the best of three bad results, which may be useful in situations with poor or variable observing conditions or when changing centering routines on a dataset-by-dataset basis is impractical.

This investigation also highlights the importance of accuracy versus precision. Figure 2.8 shows that, when working with asymmetric PRFs, Gaussian centering is less accurate, but in Stevenson et al. (2010) it does produce better results. In this case the precision allows us always to select the same subpixels in our interpolated photometry (Harrington et al., 2007), minimizing the variance in flux, regardless of maximizing the incoming flux recorded. In cases of lower S/N, or in cases where accuracy matters, such as astrometry, the other routines will become increasingly useful.

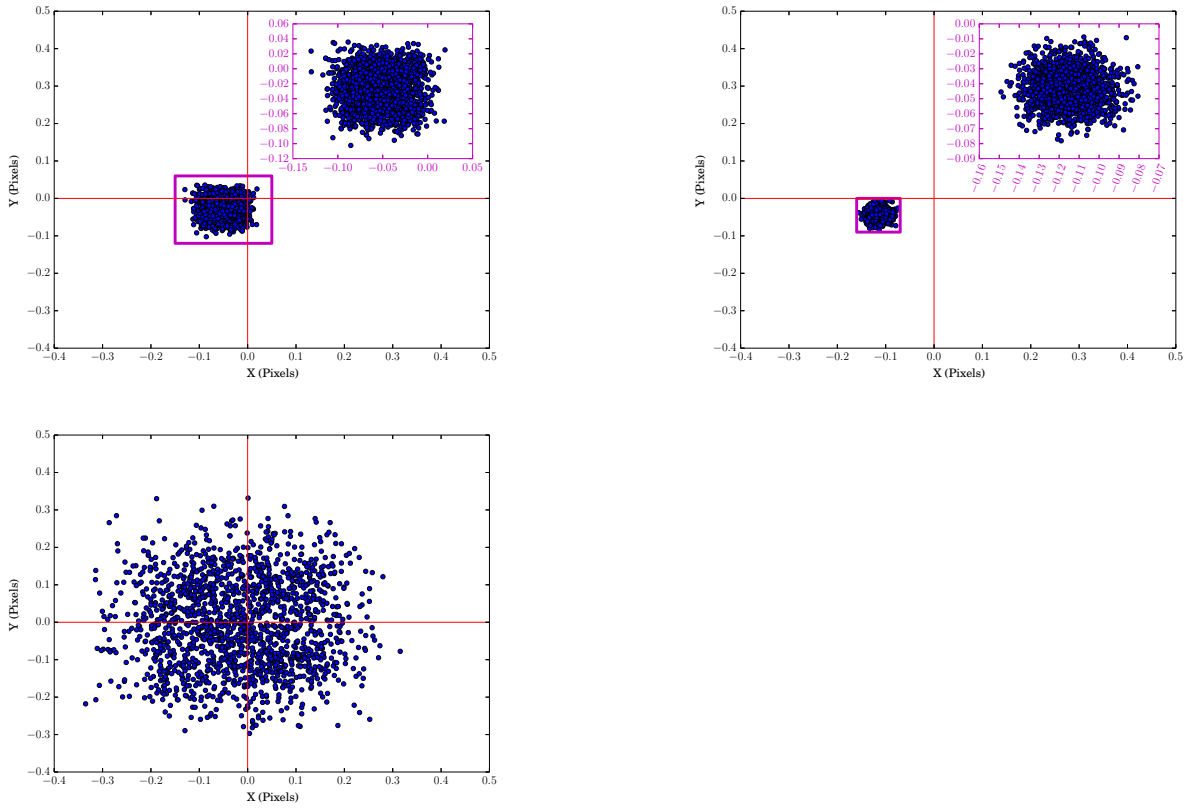

Figure 2.9: Routine precision at S/N = 60 on the 8 μm PRF. Top: The residuals from asymmetry centering. Middle: The residuals from Gaussian centering. Bottom: The residuals from Center-of-Light centering. Least asymmetery is more accurate but less precise than Gaussian centering, while Center-of-light performs worst of all. Note the axes are the same scale, but the subfigures are a larger view of the magenta square and differ in scale to provide further detail. The red lines indicate the zero point.

In the future it would be useful to investigate the effect that statistical weighting has on asymmetry and Gaussian centering. It is possible that error estimates on individual pixels could improve centering. Using unequal weights may be problematic, as a slightly wrong weight would pull the centering routine toward a wrong result, an effect that is hard to detect in datasets with unknown centers.

This work has application in a variety of areas requiring high accuracy, such as solar system orbit determination and low-signal-to-noise light curve measurements. Many photometric investigations are limited by the quality of centering. This work was developed as part of the *Spitzer* Exoplanet Target of Opportunity Program, and substantially improved the results of Stevenson et al. (2010), Campo et al. (2011), Nymeyer et al. (2011), and subsequent papers.

CHAPTER 3: ADDITIONAL METHODOLOGY FOR ANALYZING LOW SIGNAL-TO-NOISE ASTRONOMICAL DATA

Introduction

When conducting scientific observations and analysis there is often specific circumstances in which specialized routines will out perform standard analysis techniques. We often do not include these routines in the discussion of a paper as they are only a stepping stone, or may only be relevant to specific data sets. Our work in these areas may best be described as applied mathematics, but discussion of their development may aid a future researcher, and gives insight into our ability to interpret mathematical techniques and apply it in the context of astronomical observation. In this chapter we outline both techniques we frequently use, and those which have had niche uses. Additionally, some of the techniques in this chapter we have experimented with but have not found application for in our work. In these cases we hope to further develop these routines into workable analysis packages in the future.

The objective is to maximize the precision and scientific return from lightcurve analysis in order to characterize physical properties of anstronomical objects. This is accomplished by employing a series of tools developed to maximize the data return from lightcurve observations. These tools have been summarized in Lust et al. (2011) and include: (1) Further developments in the area of determining the center of a distribution of light (2) a new application of Bayesian statistics for characterizing the noise, refining the SNR, and qualitatively investigating signals and systematics, (3) the application of wavelet period analysis to lightcurves to characterize how periodicities are changing in time or identifying specific features present, and (4) The interpretation of routines using Szego polynomials for approximating frequencies in the asteroid lightcurve data.

Centering

Chapter 2 reviewed the differences between the commonly used methods for centering, center-of-light and fitting a Gaussian, and introduced a third technique least asymmetry. Each proved to be useful under differing circumstances, but for most scenarios fitting a Gaussian or least asymmetry was preferred. Though we did go to great lengths to simulate realistic noise and systematic errors, the work was specialized to the case of space telescopes where there are no atmospheric effects. Many of the qualitative differences of the routines will still hold when an atmosphere is present. Least asymmetry especially performs well under these conditions as it does not search for specific features, but rather tries to find a balance in the shape of the distribution. Frequently however a turbulent atmosphere will cause streaks, or multi-modal distributions. In these scenarios our routines will perform adequately but not ideally. We developed a routine called peak convolution which has proven to produce better signal to noise lightcuves for some observations.

The peak convolution routine begins with an image which has been trimmed such that only the object in question is in the frame, as well as enough background for a sampling of the sky brightness. In normal circumstances the width of the trimmed image is three to five times the diameter of the circle (known as the aperture) inside which the flux is summed. This smaller image (henceforth called the view) is then bi-linearly interpolated in a flux conserving manner by a desired factor. For example a re-sampling by a factor of five will give a sub pixel tolerance of 0.2, and a factor of ten will give a tolerance of 0.1. A higher interpolation factor will give provide more fine tuning in placing the aperture, but comes at the expense of speed. Bi-linear interpolation itself is fairly quick, but if it must be done over thousands of images the difference in scaling factor may become a consideration.

Next a binary aperture mask must be created for the desired aperture diameter with a one or two pixel boundary and scaled by the same factor used in creating the view. The values inside the aperture should be set to one, while those outside set to zero. This mask is then convolved with the view of the astronomical object to produce a new array which we call the convolution map. The position of the maximum value in the convolution map, controlling for hot pixels significantly above the flux of the star, represents the location in the view which has the maximum photometry at the given aperture size. The value at each position in the convolution map is the photometry value obtained by placing the aperture at that location. Thus, the convolution map provides the highest value of photometry as well as the centering location.

If the noise in the image is greatly dominated by noise from the photon statistics, (as opposed to systematic sources), then the location of highest photometry in the convolution map will also correspond to the location of highest signal to noise. If there are other significant sources of noise, perhaps from a known bias pattern in the detector, a weighting mask the same shape as the view can be created and applied to the convolution map such that the routine will search for the highest signal to noise instead of the largest photometric value.

This procedure offers many compelling features. Performing a convolution is a widely implemented, highly optimized procedure which can be performed very quickly. Peak convolution has the added benefit of conducting centering and measuring photometry in one step. This saves some computational effort, but certainly saves computational complexity in the implementation and usage. Additionally, because this method combines both steps in one, it is able to find the preferred solution regardless of the shape of the light distribution. This gives it a certain amount of resistance to noisy conditions and atmospheric blurring. In contrast, a center-of-light calculation is a weighted average which may be skewed due to noise and shape of distribution, and least asymmetry and fitting a Gaussian will tend to skew toward the peak of the distribution (Gaussian more than asymmetry).

Wavelet Analysis

In the following sections we will be discussing analysis tools which are in part or in whole based upon wavelet analysis. It is useful to digress into a description of what wavelet analysis is, how it works, and why it is useful before getting into particular applications of wavelet analysis. While not intended to be a complete presentation of the topic, we aim to convey the core ideas and outline the similarities and differences with other linear transform based analysis.

Samples obtained from observations are time averages of signals over some real continuous function which can be decomposed onto a set of basis vectors. Many are already familiar with this concept from calculus where a vector can be represented with a set of basis vectors (i,j,k), or from Fourier analysis where any square integrable function can be represented as a sum of trigonometric functions. Wavelet analysis is an alternative way to decompose signals in which the basis vectors are constructed from a wavelet function. Unlike Fourier analysis where the basis vectors span the entire dataset, wavelets are localized in time.

A wavelet transform may use localized sines and cosines to deconstruct a signal, but is not restricted to these functions. There are many functions that can serve as a basis set for a wavelet transform. Each of these wavelets share the property that they asymptote to zero at positive and negative infinity, and integrating to zero. The choice of which wavelet basis to use in a transform depends on the application of the transform. This is analogous to representing a digital signal with a series of delta functions or Fourier series. Both representations can reproduce the input data points, but one may be better at representing the behavior or trend of the data. These features of the wavelet transform allow investigation of features at different scales without changing or depending on the data in the rest of the observation; i.e. ignore a noisy patch, or identify a short lived but significant variation (such as the orbit of a satellite about an asteroid, or the eclipse of star by a planet) without requiring an extremely large number of coefficients.

The most straightforward wavelet to understand is the Haar wavelet (Haar, 1910), which is simply a piece-wise step function as depicted in Figure 3.1. Any signal can be thought of as a sum of step functions of various sizes. This idea can then be extended into different structures which are similarly localized, such as the so called mexican hat wavelet built from the second derivative of a Gaussian (Ryan, 1994) shown in Figure 3.2. This idea of a localized basis is similar to the concept of a windowed Fourier transform, but has the ability to use a non trigonometric basis as well as having the size of the window correlated to the scale of the feature being investigated.

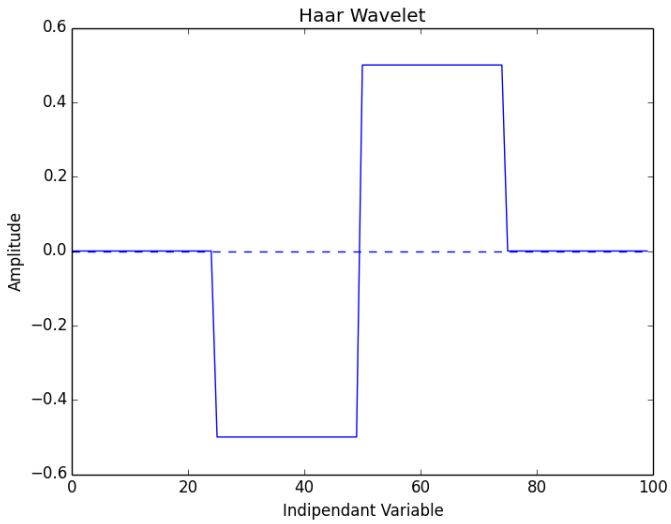

Figure 3.1: Example of a Haar wavelet.

One of the strengths of wavelet analysis is the ability to choose the best basis for the type of feature being investigated out of many possible bases. Any wavelet basis may be used, but the number and interpretation of the basis coefficients will change with different basis. The wavelet basis, called the mother wavelet, is scaled to each resolution level of the data. This scaling may be done such that the transform may or may not have overlapping support of the basis vectors. For the case of a wavelet series on discrete data, non overlapping support ensures a complete reconstruction of the original signal while overlapping support is sometimes desirable for investigating specific scales or

details present in the data. The inner product between the scaled, known as the daughter, wavelet and the signal is computed and stored as a coefficient. The daughter wavelet is then translated along the independent axis, time in one dimension or position in two, and the inner product is computed at each location to generate the corresponding wavelet coefficient. Equation 3.1 shows the equation for an arbitrary wavelet with a scaling parameter a and time localization parameter b. Individual wavelets with have particular implementations of the function Ψ but they will all have a scaling and translation parameter. The procedure for calculating the wavelet coefficients is given in Equation 3.2. For completeness Equation 3.3 provides a way to reconstruct a transformed signal with the wavelet used in deconstruction as well was the wavelet coefficients.

$$\Psi_{a,b}(t) = \frac{1}{\sqrt{a}}\Psi(\frac{t-b}{a}) \tag{3.1}$$

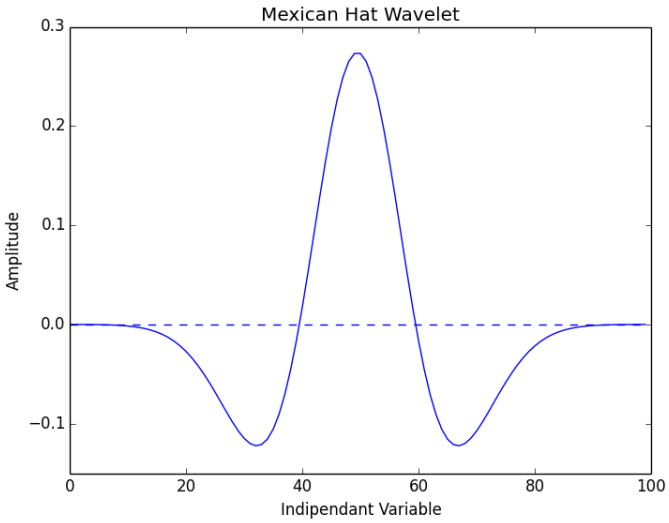

Figure 3.2: Example of a Mexican Hat wavelet.

$$WT_{\Psi}[x](a,b) = \langle x, \Psi_{a,b} \rangle = \int_{\mathbb{R}} x(t)\Psi_{a,b}(t)dt \tag{3.2}$$

$$x_a(t) = \int_{\mathbb{R}} WT_{\Psi}[x](a,b) \cdot \Psi_{a,b}(t)dt \tag{3.3}$$

Like Fourier transforms, wavelet transforms may be computed with a continuous wavelet transform (CWT) or quickly with a discrete wavelet transform (DWT), each of which have particular applications. DWTs are able to transform a data vector to a series of coefficients to the wavelet basis, but only out to a certain level determined by the length of the data and shape of the wavelet basis. These transforms are well suited for applications such as data compression, denoising, and to a limited extent frequency analysis. CWTs can still be used on discretely sampled data, since we assume it samples a continuous function, but gives us some flexibility that DWTs do not offer, such as overlapping support and fine tuning scale (frequency is one example of scale) response. Because wavelets are localized waves, they must be shifted in time to sample the entire data vector. In a DWT these shifts must occur such that the end of one wave is the beginning of the next. With CWT the wavelet is a continuous function parameterized by time and scale, and thus can accept any time index. This overlapping of support in the wavelet basis allows us to quickly and easily determine when a particular signal is present in the data. Also as a consequence of non overlapping wavelets in a DWT, only particular scales can be investigated, as the length of the data must be evenly divisible by the length of the wavelet at the particular scale. This can be mitigated by zero padding the data to match the appropriate scale but may cause aliasing at the boundaries; however, there is still a fundamental frequency which can be investigated due to the sampling rate and discrete wavelet. A CWT, as mentioned, is characterized by time; as such, we can use the knowledge of when a data point was sampled to construct the appropriate wavelet and sample any scale. This makes a CWT ideal for scale and, with particular wavelets, frequency analysis.

In a discrete wavelet transform there are only a finite number of wavelet coefficients for each signal, related to its length. A complete deconstruction of the signal is still possible by making use of an additional scaling function, the father wavelet. This is introduced to preserve the overall scaling of the signal, and ensure a signal encoded with a finite number of coefficients can be completely reconstructed. Each particular wavelet has a corresponding father wavelet uniquely designed to compliment it. The father wavelet is most closely analogous to the zero frequency of a Fourier transform where the power corresponds to the median value of the function, but contrasts in the fact that the father wavelet may also be localized in time, providing a different scale at different time intervals.

The final result of a wavelet transformation is a two dimensional data set, with one axis corresponding to time, the second corresponding to scale, and the strength of the coefficient corresponding to how well the data matches the wavelet. This two dimensional representation is referred to as a scaleogram. The time axis allows us to localize events in time, while the scale allows us to investigate features of the data which occur on different time scales, i.e. noise will occur on the shortest time scales while natural features in the data such as the eclipse events of an exo-planet or rotational period of an asteroid occur over a much longer time, and thus will be represented in a different scale.

Denoising

Signals from astronomical sources can be thought of as some real signal plus a noise term as shown in Equation 3.4. We make the assumption that the noise is normally distributed, which holds for all white noise, and when the photon count (Possion noise) is high. In denoising we seek to find the values of x_i by removing the noise from y_i. To separate the various components of the signal, it is decomposed into a corresponding series representation with a wavelet transform. Equation 3.5

shows this decomposition at each wavelet (scale) level with the index representing the independent axis. We are most interested in the scale levels, henceforth called levels, which correspond to the shortest time lengths. We will refer to the lowest level as one, with larger scales corresponding to larger numbers up to a maximum number corresponding to the length of the data-set. The coefficients up to a certain level, where we expect signal to exist, correspond to only with the noise term in Equation 3.4. Because a wavelet transform is a linear transform Equation 3.5, like Equation 3.4, has a coefficient that corresponds to reality which is contaminated by additive noise noise.

The denoising process may not alter the statistical significance of a measurement once the covariance of the transformed data is taken into account. Even when this is the case, denoising is still a powerful and useful tool. It can be useful to identify patterns of concealed signals which where not obvious in the original data, such as the discovery of two planets in the GJ 436 planetary system (Stevenson et al., 2012b). We initially had evidence of one unknown planet in the system, but by denoising the data a secondary planetary candidate was identified. This discovery was supported by performing transit modeling on the original data near the location identified in the denoised data. Denoised data-sets can also be used to find unknown systematics, generate better point-spread-functions from image field stars, aid in positioning when determining the asymmetric position of a solar system body, and identifying non-obvious trends within data-sets.

$$Y_i = x_i + \mathcal{N}(0, \sigma^2) \tag{3.4}$$

$$d_i = \theta_i + \mathcal{N}(0, \sigma^2) \tag{3.5}$$

Shrinkage and Thresholding

A wavelet coefficient is the amount of signal which is represented with a particular wavelet basis. Because of this, if we believe the portion of the signal represented on that particular basis is comprised partially or predominantly with noise, shrinking or eliminating the coefficients will result in decreased contribution from noise after performing an inverse transform. Routines have been developed for determining which coefficients should be modified such that the denoised signal remains consistent with the measured values. These routines commonly employ either determining a shrinkage factor for each coefficient, or determining a threshold value below which the coefficients are considered noise and eliminated, and above which the coefficients may or may not be altered depending on the routine. We outline the pros and cons of several common techniques while noting this is not an exhaustive list.

Baysean Linear Shrinkage We begin by describing a denoising strategy based on the standard Bayesian formulation given in Equation 3.6. This equation tells us that if we have the probability distribution of some measured quantity B depending on an unknown property A, along with a prior estimate of the distribution function associated with A, we can estimate the unknown quantity A as the maximum likelihood of the probability distribution of A given measurements B. This formulation can then be applied in the context of determining wavelet coefficients shown in Equation 3.5. The measured quantity d will have a distribution given by 3.7, note that the variance of this distribution is the same as that estimated on the observed data as should be expected with a linear transform. We then make the assumption that our denoised coefficients θ will be distributed according to equation 3.8. Because the probability density function $P(B)$ in Equation 5.1 acts only as a scaling constant, it can be ignored when calculating the value which gives the maximum

likelihood for θ as the absolute value does not matter, only the relative nature of the distribution is important. Thus by substituting Equations 3.7 and 3.8 into 5.1 and solving for the argument of maximum likelihood we get Equation 3.9. This is known as linear shrinkage. By estimating parameters for σ from the collected data (photon noise, read noise, background sky flux level), and Σ, ϵ from the distribution of coefficients, each coefficient is shrunk by a fixed factor.

$$P(A|B) = \frac{P(B|A) \cdot P(A)}{P(B)} \tag{3.6}$$

$$d \sim \mathcal{N}(\theta, \sigma^2) \tag{3.7}$$

$$\theta \sim \mathcal{N}(\epsilon, \Sigma^2) \tag{3.8}$$

$$\theta_i = \frac{\sigma^2 \cdot \Sigma^2}{\Sigma^2 + \sigma^2} \cdot [\frac{d_i}{\sigma^2} + \frac{\epsilon}{\Sigma^2}] \tag{3.9}$$

This technique demonstrates the shrinkage of coefficients where the change in each coefficient is related to a polynomial function. This particular routine is conservative at denoising, due to the linear change in coefficients, but is presented as a demonstration of the concepts behind systematically identifying and modifying coefficients. There are similar routines which perform quadratic, or other nonlinear shrinkage, which are more agressive in denoising, but are beyond the simple introduction provided by this chapter. We offer the caveat that this technique can only be utilized when there is an estimate for the prior distribution of points (a model) and is therefore most useful in situations of denoising known distributions such as a Gaussian.

Thresholding An alternative to modifying wavelet coefficients through Bayesian inference is to establish a threshold and only modify those coefficients which are not beyond that threshold. Various wavelet thresholding techniques exist, each with their own advantages and disadvantages. Two common methods for suppressing noise are hard and soft universal thresholding and are defined, respectively, as follows:

$$\omega = yI(|y| > T)\omega = sgn(y)(|y| - T)I(|y| > T), \tag{3.10}$$

where y (ω) are the original (denoised) wavelet coefficients at a particular level, I is the Indicator function, and T is some threshold limit. In both instances, if a particular wavelet coefficient, y_i, is less than T, then $\omega_i = 0$. With hard thresholding, the remaining coefficients are unaltered; however, soft thresholding shrinks these coefficients by the threshold limit.

There are many ways to estimate the value of T, including *VisuShrink*, *SURE Shrink*, and *Bayes Shrink*. The last technique is an adaptive data-driven threshold that estimates T at each level of decomposition by minimizing the Bayes Risk (Chang et al., 2000) and is the method chosen for this paper. *Bayes Shrink* employs soft thresholding because its optimal estimator yields a smaller risk that hard-thresholding's estimator.

The optimal threshold value is determined as follows, following the description by Chang et al. (2000). In some instances, the noise variance, σ^2, may be known *a priori*. If this is not the case, it is estimated from the robust median estimator (Donoho & Johnstone (1994), Donoho & Johnstone (1995)):

$$\sigma = \frac{Median(|Y_1(y)|)}{0.6745}, \tag{3.11}$$

where $Y_1(y)$ represents the wavelet coefficients, y, at the lowest level of decomposition. Next, we estimate the variance of $Y(y)$ at a particular level j, assuming zero mean, by:

$$\sigma_j^2 = \frac{1}{n} \sum_{i=1}^{n} Y_j^2(y_i). \tag{3.12}$$

where n is the number of wavelet coefficients at that level. Our observation model tells us that $\sigma_j^2 = \sigma_x^2 + \sigma^2$ so, to account for the case where $\sigma^2 > \sigma_j^2$, we calculate the standard deviation as follows:

$$\sigma_x = \sqrt{max(\sigma_j^2 - \sigma^2, 0)}. \tag{3.13}$$

Finally, the optimal threshold at a particular level is determined by:

$$T_j = \frac{\sigma^2}{\sigma_x}. \tag{3.14}$$

In the event that $\sigma^2 > \sigma_j^2$ ($T_j = \infty$), all of the wavelet coefficients are set to zero.

Error Analysis

Error analysis is quite important when measuring physical phenomena, as it places meaningful bounds on measured quantities and better informing future research and analysis. To explore error propagation of observational data with errors through a wavelet transform and subsiquent coefficient filtering we will look at the transformation using the notation of linear algebra. The vector of observed data points is denoted by X and is decomposed into the wavelet basis using the wavelet matrix W as shown in Equation 3.15.

$$Y = WX. \tag{3.15}$$

As noted in section 3 the vector of wavelet coefficients Y represent the transformed data along with noise. Certain coefficients in the Y vector will be changed such that in the inverse transform their contribution to the data-set will be modified or eliminated. This modification is conducted by means of a filter matrix Λ shown in Equation 3.16.

$$\hat{Y} = \Lambda Y. \tag{3.16}$$

The denoised signal is them obtained by performing an inverse wavelet transform on our filtered data (Equation 3.17).

$$\hat{X} = W^T \hat{Y} \tag{3.17}$$

Equation 3.18 gives the complete transform and denoising process.

$$\hat{X} = W^T \Lambda W X \tag{3.18}$$

With the denoising process laid out in terms of linear algebra transformations we can begin to address the question of how to propagate errors though this transformation. Because we have filtered our wavelet coefficients using Λ we have introduced correlations in adjacent elements. This means that unlike with our original observations X in which we need only concern ourself with the vector of uncorrelated variances σ^2 where σ is the standard deviation of our measurement error, $\hat{X}$ will have a covariance matrix Ω. The task of error propegation becomes one of determining Ω.

In general the covarance of a vector $\hat{X}$ can be found using equation 3.19 where E is the expectation value operator.

$$\Omega = Cov(\hat{X}) = E(\hat{x}\hat{x}^T) \tag{3.19}$$

In general $\hat{X}$ does not have a known functional representation of the distribution a priori making it difficult, if not impossible to calculate the covariance directly. However, Equation 3.18 gives us an alternative represenation for $\hat{X}$ in terms of our observed data X. With this substitution we obtain equation 3.20.

$$\Omega = E(W^T \Lambda W X X^T W^T \Lambda^T W) \tag{3.20}$$

Because the expectation value only depends on the vector X we obtain Equation 3.21.

$$\Omega = W^T \Lambda W E(XX^T) W^T \Lambda^T W \tag{3.21}$$

We howevef make note that $E(XX^T)$ is the covarance matrix of the vector X. Additionally, subsequent observations of X are uncorrelated with variances given by the vector σ^2. Thus, this vector corresponds to a covarance matrix Σ^2 with the vector σ^2 along the diagonal elements. Equation 3.21 can then be rewritten as Equation 3.22.

$$\Omega = W^T \Lambda W \Sigma^2 W^T \Lambda^T W \tag{3.22}$$

Each term in Equation 3.22 is a square matrix, and that after the algebreic calculations, will result in a square matrix. This is an important check as we expect a covariance matrix to be square with dimensions corresponding to the length of our data. All of the values in each matrix are either known or can be computed from the observed data. Evaluating Ω becomes a strait forward, though possibly long, linear algebra calculation.

With the covariance matrix and denoised values it is possible to evaluate how some physical model Z fits observed data. A commonly used standard metric for making this comparison is the chi-squared, χ^2, value. The most familar formulation for this evaluation is given in Equation 3.23.

$$\chi^2 = \sum_{i=0}^{N} \frac{(Z_i - X_i)^2}{\sigma_i^2} \tag{3.23}$$

Unlike the case with uncorrelated errors we must take into account how the correlations between points will affect the calculation of χ^2. We then look at a more generalized formulation of a χ^2 distribution, given $\hat{X}$ and Ω, shown in Equation 3.24.

$$\chi^2 = \hat{X}^T \Omega^{-1} \hat{X} \tag{3.24}$$

If we then want to compare some model Z, which depends on some other parameters to be varied, we modify Equation 3.24 similarly to Equation 3.23 to get Equation 3.25.

$$\chi^2 = (Z - \hat{X})^T \Omega^{-1} (Z - \hat{X}) \tag{3.25}$$

With this formulation we can use our denoised data along with our covariance estimates to perform model fits independently or in conjunction with other methodologies such as Markov-Chain Monte Carlo analysis.

Time-series image Denoising (TiDe)

The denoising techniques that we have outlined are established techniques used in a wide variety of fields. When applying denoising to astronomical observations, the natural idea would be to make some assumption about the shape of the point spread function, and denoise each frame. While this approach is valid, frames may have relatively small dimensions leading to poor statistical sampling, and edge pixels may contribute a significant amount of information.

We propose an alternative approach which we call Time-series Image Denoising, or TiDe (pronounced as tidy). In this approach we make the observation that if the center of the point spread changes remains approximately stable, then each pixel will represent its own one dimensional noisy time series. By working with individual pixels we gain the knowledge that short term variations should be relatively small, and the signal will be largely consistent over the whole series. The temporal domain gives us many more observations on which to base our statistical estimates of denoising parameters, in addition to containing only two endpoints which are of negligible importance to the overall signal. The method also allows the correlation of scale levels with temporal durations ensuring levels which correspond with the signal being investigated will not be altered. By denoising pixels separately we are also able to deal with individual systematics a particular pixel may exhibit.

The denoised frames, generated by TiDe on each pixel, have many benefits over their noisy counterparts. First the centering will improve as the uncertainty in the center has decreased. This will benefit placing photometric apertures, and identifying systematics such as the bliss method (Stevenson et al. (2010)). Another area where TiDe may be useful is in generating point-spread-functions from numerous field stars for the purpose of star subtraction. This is often done in cases where an object being observed lies in a dense star field and systematic contributions from stars need to be identified and removed.

Application of Denoising Example

A practical application of denoising can be found by investigating the analysis of observations taken of the Kepler-9 planetary system. It is comprised of two Saturn-sized exoplanets orbiting a Sun-like, G2 star close to their mutual 2:1 orbital resonance (periods = 19.2 and 38.9 days for Kepler-9b and Kepler-9c, respectively) and a super-Earth-sized exoplanet (Kepler-9d) on a brisk $\sim$1.6-day period. In this example we use data published by Holman et al. (2010) are publicly available for download in three FITS files (one for each quarter of observation). The files contain long-cadence photometric data ($\sim$30-minute exposures) in the optical I-band spanning seven months, from 13 May 2009 to 16 December 2009, that have been processed with the Kepler pipeline. Figure 3.3 displays the normalized light curves from each quarter. There are large gaps in observing between quarters and smaller gaps within the second quarter.

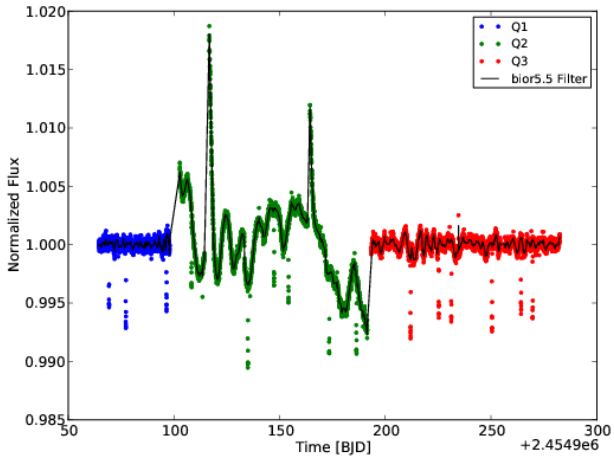

Figure 3.3: Normalized light curves spanning three quarters, depicted in blue, green, and red. The black line is the result of soft thresholding using a biorthogonal 5.5 wavelet and is used to detrend the data. The transits of Kepler-9b and Kepler-9c are clearly visible as the periodic dips in the normalized flux within the data.

Kepler-9 is an M dwarf star and is mildly active, particularly in the second quarter of observing (see Figure 3.3). In order to detrend the light curve without reducing the significance of the transits, we applied a simple median filter to the normalized data using a sliding window of 25 points (750 minutes) so that, at any one time, less than one third of the windowed points belong to a transit event. As a comparison we perform the same de-trending by using wavelet thresholding on the out-of-transit data to generate a denoised light curve.

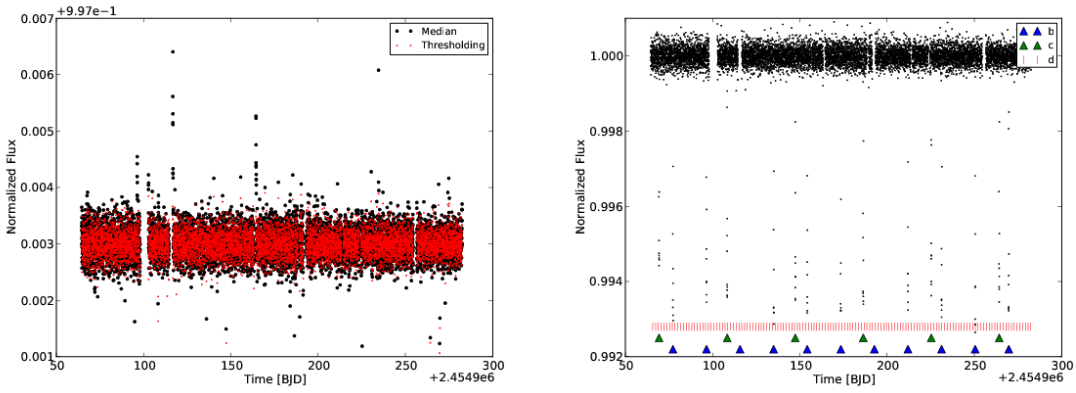

Figure 3.4: *Left panel:* Magnified detrended light curves using median filtering (black) and wavelet thresholding (red). The latter produces less scatter. *Right panel:* Full detrended light curve of Kepler-9 using wavelet thresholding. The blue and green triangles indicate transits of Kepler-9b and Kepler-9c, respectively. The red vertical lines denote Kepler-9d transits that are too weak to be seen individually.

Figure 3.4 shows the results of the systematic de-trending. The black dots are the results of the median filter, with a standard deviation of ≈ 260 ppm, while the red shows the de-noised lightcurve with a standard deviation of ≈ 215 ppm. Even without the measurements of standard deviation it is easy to see that the red dots fall inside a smaller region than the black. Also notably, the denoising process was able to remove two spikes in brightness that the median filter could not. In a median filter, new points are chosen as the median value of the group surrounding each of the original data points. Thus if there is a sharp discontinuity it will be reduced in amplitude but not eliminated unless a wide enough grouping of points were selected in the median process. This would however

effectively destroy any signal present withing the data. Wavelets however are localized, and a sharp discontinuity will simply show up as a single coefficient at the appropriate length scale in the transform. If this coefficient is eliminated, then the discontinuity will be removed in the inverse transform while preserving all the coefficients which correspond to actual signal. In the right hand image of Figure 3.4 we show the fully detrended data using wavelet denoising and demonstrate that the process did not remove the eclipses from the data.

Wavelet Period Analysis and Feature Detection

Period Analysis

Because of the clear connection between periodicities and trigonometric functions, Fourier transforms are frequently used in analysis. Wavelet analysis is an alternative linear transform for the same set of square integrable functions, but differ in key ways which make them ideal for analyzing lightcurves. With Fourier transforms the signal is decomposed onto trigonometric bases with support on the whole time domain, meaning many basis vectors (coefficients) are needed to represent the signal. This is especially apparent when there is a slow time varying change, such as a shifting period, present in the data. As discussed in section 3 wavelets use a system of basis functions which are localized in the time domain with the scale of the basis function proportional to the size of the feature, i.e. frequency, in consideration.

As stated, there are many different types of wavelet transforms available. For most lightcurve analysis we choose to used a specialized continuous wavelet transform outlined in Foster (1996). This technique, known as a weighted wavelet Z transform (WWZ), uses a methodology known as date projection to deal with unevenly sampled data, which is ideal as many astronomical data sources do not have constant cadence and contain gaps between observations. The WWZ is constructed

from decaying sign and cosine waves, which allows for identifications of periodic behavior, while still localizing these periodicities in time. Since it is a continuous wavelet transform, it has overlapping support which provides good investigative coverage. This type of transform is not ideal for denoising as the inverse transform is ill posed, but for investigating periodicities or features there is no need to perform an inverse transform.

We will first demonstrate the WWZ transform on the lightcurve of the asteroid 1022 Olympiada. We again obtain the data from Warner et al. (2009a). In figure 3.5a we see the lightcurve for (1022) Olympiada. The results of the transformation are shown in figure 3.5b. This is a two dimensional contour plot with an x axis of time and a y axis of frequency. We can clearly identify the primary and half frequency from the rotation of the body. If we are concerned with only the frequencies and not when they occur in time, we can average over the time axis to produce a power spectrum analogous to a Fourier transform, which can be seen in figure 3.5c. Though the period of this lightcurve is easy to identify by eye, and would be just as clear with a Fourier transform, the objective here is to highlight the effectiveness and functionality of the routine when the results were easy to identify.

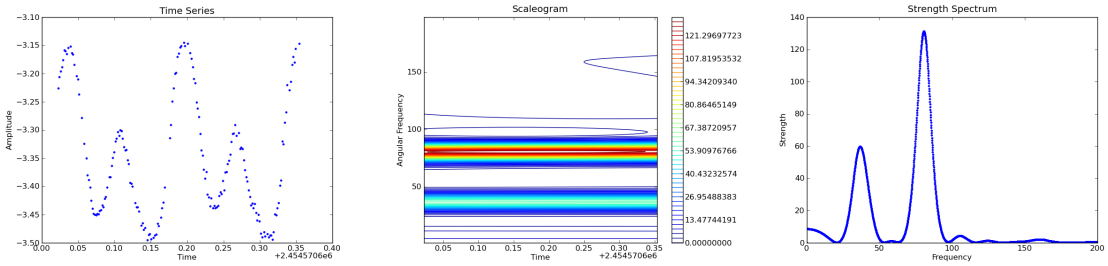

(a) Time (b) Scaleogram (c) Power Spectrum

Figure 3.5: Wavelet transform for (1022) Olympiada. Data from Warner et al. (2009a)

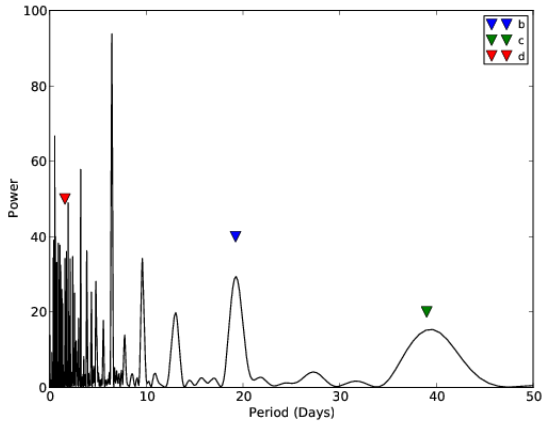

Figure 3.6: Kepler-9 periodogram using the Lomb-Scargle method for unevenly sampled data. The colored triangles depict the true periods of the three exoplanets.

For a more in-depth example, in which the periodicities of the data-set are not so defined, we return to the Kepler-9 system used in section 3. A fast Fourier transform was performed on the lightcurve, the results of which can be seen in Figure 3.6. The periodogram exhibits relatively strong peaks at the known periods of Kepler-9b and Kepler-9c (as indicated) but the strongest peak occurs at a period of 6.45 days. This value is a harmonic of both periods, which is why it is so strong. The period ratio of this peak is 6:1 for Kepler-9c and 3:1 for Kepler-9b. The next strongest peak longward of 6.45 days occurs 9.6 days and is the 4:2:1 harmonic. The periodogram also shows some power near 13 days, the 3:1 harmonic with Kepler-9c. The numerous narrow peaks that plague the periodogram around 5 days and shorter are even weaker harmonics. We conclude that this periodogram alone is insufficient to confirm the orbital periods of any of Kepler-9's exoplanets because of the tendency of this method to pick up harmonics of the dominate periodicites.

We next used the WWZ method to transform the Kepler-9 data-set, as shown in Figure 3.7. Looking at the scaleogram (Figure 3.7a) the features of Kepler-9b and Kepler-9c can still be seen near 40 and 20 days respectively. When looking towards the shorter periods, the structure of the scaleogram becomes more complicated as with the fast Fourier transform in Figure 3.6. However, unlike the results from the FFT, the scaleogram shows that the harmonic power at these frequencies are localized in time. In figure 3.7b the scaleogram has been averaged over time, such that only signals which span a significant portion of the data-set are strongly weighted. This figure shows that unlike the FFT, the lower power harmonics are eliminated, while the strongest harmonic is reduced in strength. The Feature of Kepler-9d is even detectable near 2 days, a feature which was completely hidden in the power spectrum of the Fourier transform. We can thus conclude that this transform allows quicker and more straight-forward identification of relevant periods in astronomical data sets.

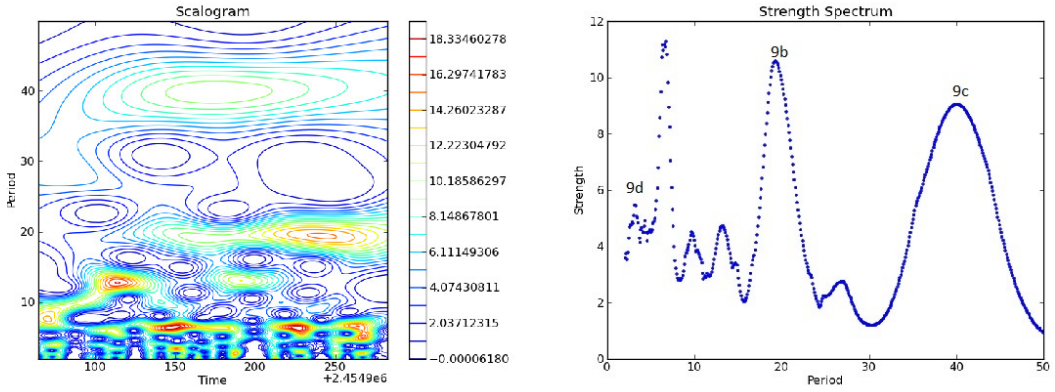

(a) Scaleogram

(b) Power Spectrum

Figure 3.7: A weighted wavelet z transform of Kepler-9, where the color represents the strength of the coefficient.

Feature Detection

Often in astronomy, it is desirable to detect localized features instead of long term patterns such as periodic behavior. These localized features may be the radio pulse from a pulsar, outburst of a comet, a signature of an exoplanet, or a satellite of asteroid eclipsing its parent body. Because the signal which is sought is localized in time, wavelet analysis again provides a powerful tool. In addition to being localized in time, the particular wavelet used in a transform can be tailored to the feature being investigated. As an example we once more return to the Kepler 9 planetary system. In this scenario we seek to identify the location of planetary transits, rather than the period at which they occur. This necessitates switching from a wavelet with periodic properties, to one similar to that in Figure 3.2 in Section 3. In particular the negative Mexican hat wavelet is chosen for its resemblance to a planetary transit in which the flux from the star decreases in a localized manor. Figure 3.8 shows the results of this wavelet transform. It is immediately clear that the high intensity regions of the scaleogram correspond to the location of transits within the Kepler 9 data-set. A wavelet specialized to the shape of a planetary transit would have an even stronger response. Similarly detecting features from other astronomical sources through a wavelet transform is strait forward provided the proper wavelet to model the signal is chosen.

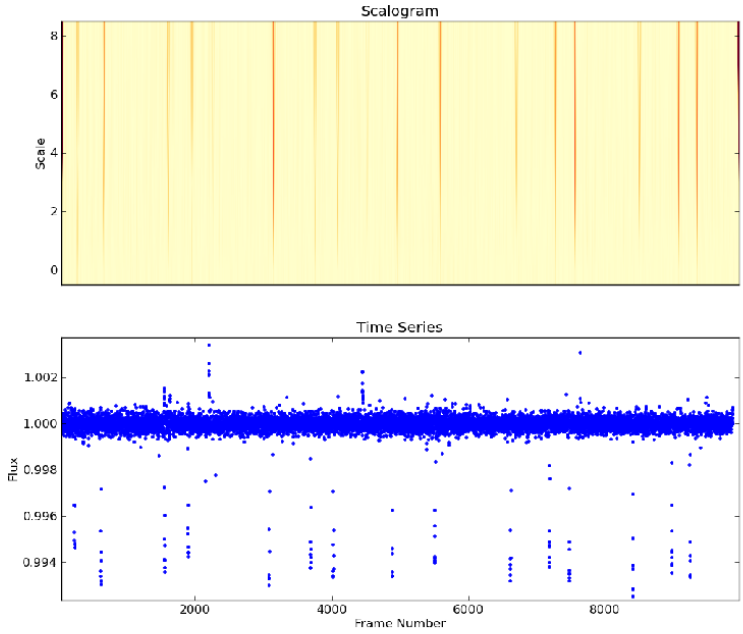

Figure 3.8: SDG wavelet transform of Kepler-9. The large coefficients seen in the scaleogram correspond in time with the dips in flux due to planetary transits

Szego Polynomial Frequency Analysis

Determining periodicities with methods such as Fourier and wavelet analysis is done by a process analogous to guess and check. The signal is projected on a basis of a particular frequency, producing a coefficient representing the prevalence of that frequency. This is reliant on testing the correct period and is sensitive to high levels of noise. Szego polynomials (Jones et al., 1990) offer an approach where the end result will asymptote to any frequencies which are present, independent of large numbers of iterations. This ensures the correct periods are investigated, and not harmonics or local phase space minima, which can lead to incorrect shape or formation models. This feature is particularly useful in the analysis of binary lightcurves or with objects in complex rotation states, where multiple non-harmonic periods will be present.

$$\rho_0(\psi;z) = 1, \rho_0^*(\psi;z) = 1, \tag{3.26}$$

$$\rho_n(\psi;z) = z\rho_{n-1}(\psi;z) + \delta_n\rho_{n-1}^*(\psi;z), n \geq 1, \tag{3.27}$$

$$\rho_n^*(\psi;z) = \bar{\delta}_n z\rho_{n-1}(\psi;z) + \rho_{n-1}^*(\psi;z), n \geq 1. \tag{3.28}$$

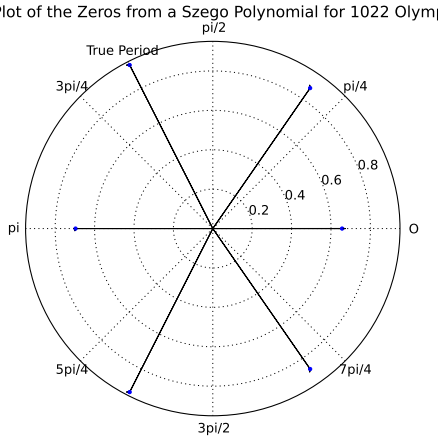

Figure 3.9: Zeros for a sixth order Szego polynomial constructed from (1022) Olympiada. Data from Warner et al. (2009a)

To begin, the input data vector is used to construct a measure such that the Szego polynomials will be orthonormal inside the unit circle on the complex plane. This measure is then used in the recurrence relations 3.26, 3.27, 3.28, where delta is built from the previous Szego polynomial coefficients and the cross correlations of our signal, to construct a polynomial of the desired order. The phase of the largest in magnitude complex zeros will asymptote to the periodicities present within the data. Because of the asymptotic nature at large numbers of observations, this routine will not return the exact periodicites present with small to moderate length data sets. It will, however, provide an approximate answer and serve as a guide to distinguishing true periodicities from harmonics and spurious results in traditional Fourier and wavelet analysis.

In Figure 3.9 we show the results from Szego polynomial analysis on the data-set of (1022) Olympiada from section 3 using a sixth degree polynomial. In this analysis, the time axis has been re-mapped such that any angular frequencies will map between zero and pi. The first thing we note is that frequencies often occur in conjugate pairs, due to this routine's insensitivity to signals propagating forward or backward in time, and thus we need only concern ourselves with results from zero to pi. Secondly, we notice that the largest modulus zero does correspond with the published frequency, giving a value for the period of 0.154 days versus 0.159 days for the published value, a difference of about 7 minutes. The data-set used in this transformation only covers two periods and thus we can expect better convergence with longer data sets.

An additional example is given with the analysis of 549 Jessonda, with data again obtained from Warner et al. (2009a). We denoised the lightcurve and created a low order Szego polynomial with this data to look for periodicities, shown in figure 3.10b. The most likely period as determined by the Szego polynomial routine was found to be 0.231 days. Using a minimizer on the original data-set, near the Szego result, we find a minimum at 0.247 days with a lightcurve shown in figure 3.10c. For comparison, the lightcurve with the published value is shown in Figure 3.10a. We find this curve likely as it is bi-modal, a typical trait of asteroid rotation curves. Subsequent communications with the original observers have indicated that they too find a period of 0.247 days to be more likely.

Conclusions and Future Work

Through out this chapter, we have described methodologies developed for the analysis of low signal-to-noise astronomical signals. Though it is not an exhaustive list, examples were provided for some possible uses for these methods.

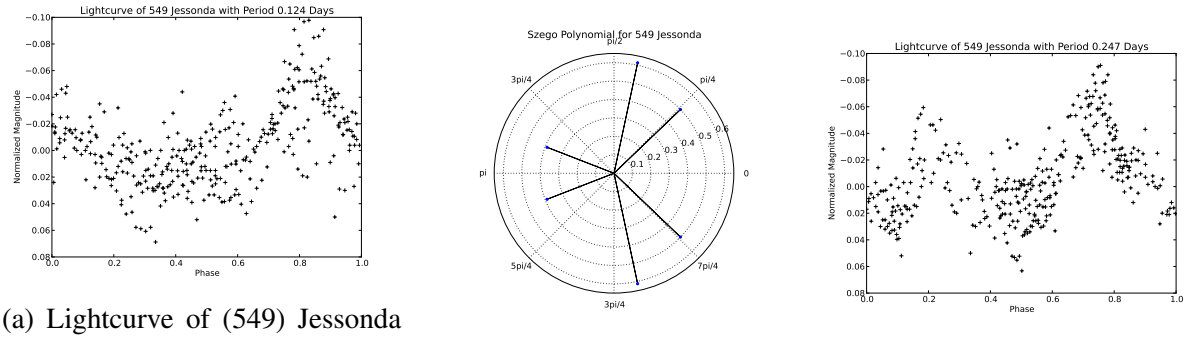

(a) Lightcurve of (549) Jessonda using the published period of 0.124 days.

(b) Szego polynomial zeros for (549) Jessonda

(c) Lightcurve of (549) Jessonda using a period of 0.247 days.

Figure 3.10: An example of finding periodicity within an asteroid lightcurve.

In centering we have provided another method for performing photometry with noisy data-sets through the use of peak convolution. This tool is especially well suited for working with ground based data, as atmospheric turbulence can cause variable and unpredictable distributions of light in an observed image. This work may be expanded by exploring the behavior of the convolution mapping. Using existing centering and minimization routines, we may find even more accurate photometric results by optimizing over the shape of the convolution map. This, in effect, would be a further interpolation of the data, but one that is informed by the overall flux, and not individual neighboring pixels.

Denoising has been shown to be a powerful tool, but one which must be used appropriately and with careful consideration. This involves selecting the appropriate shrinkage or thresholding for the problem at hand, as well as determining the thresholding limit. We have discussed different methods for denoising, such as per-frame or along the time axis, each of which offer different pros and cons. These methods can be used in varying scenarios from determining and removing systematic trends, to improving the determination of the sensitivity within a pixel.

We have discussed the math behind, and usage of, wavelet analysis. When using a wavelet based on sine waves this methodology provides a great alternative to Fourier analysis for detecting periodicities. This tool can be much more robust against aliasing, and is able to identify and handle a period which is changing in time. Though we have discussed periodic detection in terms of temporal signal, this methodology also is capable to working with spacial effects, such as cloud bands in a planetary atmosphere which may change with latitude, or in scale. By changing the wavelet uses in the analysis, the feature being investigated can be changed from periodic in nature to arbitrary structures. As an example we have shown how planetary eclipses can be detected and localized in the lightcurve of a star. It is interesting to note how the same transformation, on the same data-set, yields entirely different scientific results by simply chaining the wavelet in use. Moving forward we would like to adapt and customize this routine for detecting transits into a routine which can automatically search for eclipses in asteroid lightcurves, which may be signatures of binary objects.

Period detection with Szego polynomials is probably the least explored technique, though possibly the one with the largest potential. This method allows for quickly and easily determining periodic behavior without a brute force searching of phase space. Even with models in which the period will be dependent on other parameters of the model, Szego polynomials may allow the elimination of one dimension of phase space to search as each combination of the other parameters will produce a unique Szego polynomial, with zeros related to the periodicity. In the future we would like to see if this method could be further optimized for shorter data-sets and noisier conditions, perhaps through an application of Bayesian probabilities.

Each of these routines provide innovative ways for accessing and maximizing scientific returns from low signal-to-noise data. We will make further use of them in the following chapters to investigate physical phenomena in situations which would otherwise be difficult to make meaningful measurements.

CHAPTER 4: COMPENDIUM OF CONTRIBUTIONS IN THE FIELD OF EXOPLANET DETECTION AND CHARACTERIZATION

Introduction

In the recent past the field of detecting and characterizing extra-solar planets (exoplanet) has been a major example of the analysis of low signal-to-noise observations. In these systems, the planet's flux is tiny compared to the flux their host stars. There are two man methods for detecting and characterizing exoplanets, radial-velocity measurements and photometric measurements of transit/eclipse lightcurves. Each method contributes uniquely to our understanding of exoplanet properties. We will outline the procedure and basic science behind each method before detailing specific investigations.

Radial velocity was the first technique to successfully detect and preliminary characterize an exoplanet (Mayor & Queloz, 1995). If an object is orbiting about the star it will cause the star to apparently wobble in space, as the barycenter of the two body system will be moving though space. This wobble will cause a periodic shift in the star's spectrum, as the star alternatively moves toward and away from the observer. The magnitude of this change (due to a changing apparent velocity) is determined by the mass of the companion object, the size of its orbit, and how closely the plane of the orbit is aligned with the line of site from Earth. In this method a spectrograph is used to make repeated measurements of a stars spectrum. As the star moves relative to Earth its spectrum will shift to the right or left due to the Doppler effect. The direction of the shift is set by the objects motion toward or away from Earth, while the magnitude of the shift is related to the velocity of that motion.

With measurements of periodic variability in a stars spectra, this problem can thus be inverted to place bounds on the properties of the companions mass and orbit. Exact values cannot be determined as there is a degeneracy between the parameter indicating the angle the orbit with respect to Earth, and the mass of the object. In other words, it is impossible to know if the observed effect is due to a large planet viewed at an oblique angle such that the star moves very little from the perspective of Earth, or if the effect is directly in the line of site with Earth and the small motion is due to a small companion pulling weakly on the primary star. However if the assumption that the orbital plane is aligned with the direction of observation the minimum mass of the companion necessary to produce that wobble can be determined.

Because the inclination of a planetary system is difficult to establish, and impossible to establish with radial velocity measurements alone, the minimum mass of the companion object can only ever be obtained with this technique. Another limitation of the radial velocity technique arises from the sensitivity of spectrographs used to conduct the measurements. Detection of a companion object occurs when that object induces a large enough motion in the primary star for the shift in its spectra to be detected. Companions with low mass will only induce a tiny wobble, and will be difficult to detect. Additionally the closer a planet is to a star the larger in pull on the host star. Thus, this method will be inherently bias toward detecting planets in small orbits or larger gas giant planets, with the majority of detections coming from large close in planets.

An alternative approach to detecting and characterizing exoplanets is to monitor the brightness of a star, and watch for a characteristic dimming which is caused by the presence of an orbiting planet. In these senarios, as seen from Earth, the orbiting planet will pass in front (transit) or behind (secondary eclipse) the star. Each of these cases will cause the total amount of flux from the planetary system to dim and allow us to characterize the planet's physical properties. The transit of a planet normally causes a dip in flux of a few hendreths of a magnitude, but may be larger or smaller. This varies with the size of the planet, and the distance it is away from its star. A secondary eclipse is many times fainter than a transit, and is normally only observable with space based telescopes.

In the case of a transit, the orbiting planet moves in front of its host star and blocks a percentage of the stars visible light. This is essentially casting a tiny but perceptible shadow on the Earth. These events can constrain the sizes, masses, and orbits of the transiting exoplanets (Charbonneau et al. (2007),Winn (2009)). With a secondary eclipse the planet moves behind the star, and because the planet does not produce any of its own light the total amount of light in the visual spectrum remains unchanged. A planet however, is a radiating black body and is thus emitting infrared light. This coupled with the fact that a star emits relatively smaller percentage of its light in the infrared produces a detectable dip in the flux from the system if viewed in infrared wavelengths. When outside of an eclipse the infrared flux from both the planet and the star is detectable, but as the planet passes behind the star, the star blocks the infrared light from the planet, decreasing the total flux. These secondary eclipses enable characterization of the planet's atmosphere (if viewed in multiple infrared band-passes), orbital eccentricity of the planet, and temperature (Kallrath & Milone (2009); Demory et al. (2007)).

The transit/eclipse method for detecting and characterizing planets also has a few drawbacks. First, these events are only detectable if the orbit of the planet happens to be in line with the telescope's vantage point. This depends on the size of the star, the size of the orbit, and the inclination of the orbit. In most combinations the probability of detecting a planet is quite small, requiring observations of a large number of stars simultaneously to detect a meaningful number of planets. False detections are also a problem for this method. Many stars are very active, having both solar flares and solar spots which can increase or decrease solar flux and thus mimic the signature of a planet. Detections require many follow up observations to confirm the repeatably of the detection, or observations with different methods such as radial velocity.

Exoplanet measurements of any kind are extremely difficult as they are very low in the signal-to-noise ratio. An example of this is the 8μm bandpass measurement of eclipse depth in Campo et al. (2011) which has a signal-to-noise ratio of approximately 9. In the case of transit/eclipse photometry the flux from the star represents a background signal which may be many orders of magnitude larger than the changes to be measured. Again using Campo et al. (2011) as an example, the planet they investigated had a flux which was approximately three orders of magnitude smaller than the flux from the host star. This is further compounded by the inherent photon noise of the system, the fundamental uncertainty in the number of photons emitted at the source per unit time. This uncertainty is related to the square root of the number of photons received, and thus a larger signal will have a larger uncertainty in the absolute sense even if the signal-to-noise ratio is larger. The photon noise of the star with thus hinder the measurement of fainter signal from the planet.

Many of the routines we initially developed for use in other areas of astronomy have proven to be quite useful in enabling more accurate measurements of exoplanet systems. In the rest of this chapter we will outline the scientific results that resulted from applying our methods which includes, implementation and optimization of planetary eclipse models, exploration and characterization of systematics, interpretation of the results from our routines, and drawing scientific conclusions based on the analysis of exoplanet data.

On the Orbit of Exoplanet Wasp-12b

Campo et al. (2011) examined two secondary eclipses of the exoplanet Wasp-12b using the Infrared Array Camera (IRAC Fazio et al. (2004)) aboard the *Spitzer* space telescope (Werner et al., 2004). This is one of the hottest known planets with an equilibrium temperature around 2500k, has a period of just 1.09 days, and orbits at a distance of only roughly 0.02AU from it's primary. At almost twice the radius of Jupiter, the planet is also quite large and is larger than theoretical models predict for this planet. The close proximity of Wasp-12b it its planet should produce large tidal forces on the planet which would quickly circularize this small orbit. The non-Keplerian gravitational potential of the parent star could cause an apsidal precession of Wasp-12b on time scales that may be measurable. The differences between the timing of eclipse-transit and transit-eclipse can very over time and provide a direct measurement of the apsidal precession of the system.

Our analysis shows a secondary eclipse phase of 0.5, where 0 is the beginning of an orbit and 1 is the end, within a two sigma confidence interval (on a scale 0 to 1 across one full orbit). This agrees with other observations of the timing of the secondary eclipse done it the past by other teams, which means the timing of the secondary eclipse is not changing in time measurably. An eclipse which is not changing in time indicates that we could not detect the presence of apsidal precession. We determined the eccentricity to be 0.065 ± 0.014, which could be higher than the true value due to poor constraints on $esin(\omega)$ (where e is the eccentricity and ω is the argument of periapsis). Our results are consistent with those of a circular orbit, but apsidal precession can not be ruled out without a longer base line of observations.

High C/O Ratio and Weak Thermal Inversion in the Very Hot Atmosphere of Exoplanet Wasp-12b

Madhusudhan et al. (2011) is a continuation of the work on the Wasp-12 system. We observed the planet using multiple bands in the IRAC camera. Different wavelengths of light will penetrate different amounts in a planetary atmosphere, so by using multiple bands we were able to sample the light from differing heights within the atmosphere of Wasp-12b. This allows us to put constraints on the concentrations of chemical compounds in the atmosphere by looking at the opacity in each of the bandpasses. A strong secondary eclipse in a particular band suggests that there are no species which strongly absorb at those wavelengths. Alternatively a weak signal means we are observing a strong absorption and can characterize the chemistry of that atmospheric zone.

Our observations find low brightness temperatures in the 3.6μm and 4.5μm channels which suggests a strong absorption by CH_4 and CO respectively. Strong CO in the 4.5μm band also indicates that temperature must decrease with altitude (suggesting a lack of stratosphere) as a temperature inversion would cause CO to have emission features in the 3.6μm band which would produce a higher flux than is observed. High brightness temperature in the 5.8μm channel suggests there is low absorption from H_2O.

We use the broadband observations in a statistical retrieval technique which allows for the inference of the chemical composition and temperature structure for the observed side of the planet. This technique combines a one dimensional model with a Markov Chain Monte Carlo algorithm which computes over $4x10^6$ models, checking if there is a thermal inversion or equilibrium chemistry, and varying over a range of atomic abundances.

In our best fit model contains little water, and a large amount of methane in the atmosphere. This is inconsistent with equilibrium chemistry if the system contains the same abundances of elements as our solar system. Our observations place a strict limit on the C/O in the system and determine a value greater than one at the three sigma confidence level which is about double that of our own solar system. This may imply there are formation mechanisms for solar systems which very greatly from models based on using chemical abundances approximately those of solar abundances.

Possible thermochemical disequilibrium in the atmosphere of the exoplanet GJ 436b

In Stevenson et al. (2010) we use the techniques and methodologies from our previous exoplanet papers to observe the exoplanet GJ 436b. This planet belongs to a class of planets referred to as 'hot Neptunes' as they are about the size of Neptune, yet are much closer to their parent star, and therefore have much higher equilibrium temperatures. The host star GJ 436 is a M dwarf star, smaller cooler than our own. This provides a stronger contrast in the thermal spectrum compared to an equivalent planet orbiting around a solar type star.

We used standard photometry and image calibration in the reduction of our data. A Markov-chain Monte-Carlo routine was used to fit channel specific systematics at the same time as the parameters of the secondary eclipse. This includes a new model of the dependence of flux on the position of the star within a single pixel on the array, as well as a model of the time varying sensitivity of the array.

Our results find the phase of the secondary eclipse to be at 0.5868 ± 0.003 which is a significant improvement of the precision from previous results. We find best fit values of $0.1371^{+0.0048}_{-0.00013}$ for the eccentricity of the planets orbit, and a period of $2.6438983 \pm 1.6x10^{-6}$ days.

The resulting eclipse models were then used in conjunction with the atmospheric chemical abundances model from Madhusudhan et al. (2011) to investigate the makeup of GJ 436's atmosphere. Basic chemical equilibrium predicts H_2, H_2O, CH_4, CO, and NH_3 should be the most abundance species present in the atmosphere. Given this, chemical composition models result in H_2O and CH_4 contributing the most to the planets emission. The strong signal in the 3.6μm band along with a lack of signal in the 4.5μm band shows that the planet is deficient in methane by a factor of around

7,000 compared to what is predicted from chemical equilibrium models. We explored varying concentrations of CO_2 and CO which may create the appearance of a lack of methane, however none of these were consistent with the observed data. Other possibilities which may explain the data which include, a temerature inversion, lack of hydrogen, planet variability, and stellar activity were explored, but none could plausibly fit the observations.

The planet is tidally locked with its host star and thus receives all of its flux on one side of the planet. This level of radiation may be able to drive disequilibrium chemistry and large scale convection in the atmosphere. It is possible that vertical mixing may increase the abundance of CO in the upper atmosphere, thus reducing the CO to CH_4 ratio, or that the large solar flux is driving CH_4 to be polymerized into other hydrocarbons.

Two Nearby Sub-Earth-Sized Exoplanet Candidates in the GJ 436 System

There has long been suspicion of additional planets within the GJ 436 system, but all previous attempts to locate any planets did not produce any solid detections. Stevenson et al. (2012b) outlined one planetary candidate, preliminary named UCF-1.01, and evidence of a second planet, which we call UCF-1.02. Both of these planets appear smaller than Earth at about 0.66 Earth radii. If they share a similar density with Earth, they each would be just under a third of an Earth mass.

Observations of the GJ 436 system were carried out with the *Spitzer* space telescope and combined with data from many sources which were previously gathered on the system. The new observations were reduced using our Photometry for Orbits, Eclipses, and Transits (POET) pipeline, which performs calibrations, systematics reduction, and photometry. We also introduced a new technique called time-series image denoising (TiDe) which allows for precise centering and reduction of intra and inter pixel systematics. In TiDe the uncertainties which arise from photon noise are modeled

and reduced, such that standard centering routines are able to determine both more accurate and more precise centers. This method recognizes that with stable pointing the same (x,y) pixel location will over time represent the same portion of the stars point spread function. We therefore use the time axis along each pixel to estimate the level of noise, and use a wavelet transform to estimate its level and reduce its contribution, while leaving the larger scale signal intact. This provides more data points with which to make estimates of the noise versus the low number of points in each frame. This denoising technique produces significantly better results when subsequent routines are used on the denoised data vs denoising the individual frames.

Using previous observations of the GJ 436 system we were able to determine the period of UCF-1.01 and make a prediction of when it should occur in the future. We were able to obtain time on *Spitzer* to test our prediction, and were successfully able observe the planet transit. We were only able to obtain two non-consecutive detections of UCF-1.02 and were thus unable to determine its period. An independent analysis of all our results agreed with all of our conclusions to within 1.5σ. Confirmation of UCF-1.01 as a planet would require only a limited number of observations, but as the period of UCF-1.02 is uncertain, further investigation of the planet would require an extensive observing campaign as future prediction of when this planet will transit are currently impossible.

When claiming planetary detections, it is important to ensure the signal is not something else which is mimicking the appearance of a planetary transit. The large proper motion of the planet makes it unlikely that we are seeing a background star which periodically dims, either because it is variable, or because it is an eclipsing binary star. We also checked past observations of this area of the sky and are able to confirm there are no stars brighter than at least 9 magnitudes fainter than GJ 436. Another possibility for a false detection may arise from stellar activity in the host

star. We calculated the probability that active events which would mimic planetary transits would happen at periodic intervals and find the probability to be negligibly small. Lastly we compare the strengths of our model fits of the GJ 436 system to the null hypothesis that there are no new planets in the system. Even with a parameter which penalizes models against the complexity of including additional variables, we find higher probability in models which include both additional planets.

CHAPTER 5: OBSERVATIONS AND ANALYSIS OF ASTEROID 2577 LITVA WITH A MODIFIED BAYESIAN INFERENCE APPROACH

Introduction

Remote observations are an inexpensive way to gather information on the physical properties of near earth objects (NEOs), the understanding of which provides insights into topics ranging from solar system formation and evolution to impact mitigation. Specific physical properties such as density and porosity help to answer questions about what these bodies are made of, where they originated, how they have been modified over time, are these objects potential resources for the human space program or industrial applications, and what is the best way to deal with potential hazards. Binary asteroid systems provide an invaluable resource for measuring these properties. The orbital period of a secondary object can be used in conjunction with Kepler's equations to determine the mass of the system and when coupled with volume estimates, the bulk density of the system can be determined.

Measurements of these physical properties are heavily constrained by the quality of observations on the body, and the accuracy of the analysis of those observations. If an NEO is large, or bright, and has a large change in brightness over its rotational cycle, it is relatively easy to make high-quality measurements with a few nights of observations. With lower quality observations, either due to a fainter body or smaller observing facilities, many nights of observations may need to be combined to achieve a high enough signal-to-noise. Even with good equipment which produces

high quality measurements, NEOs are often of such small size that it is only feasible to take observations when they are quite near Earth and at their brightest. Because the mutual orbits only keep these objects near Earth for a short periods, many different apparitions are often need to be combined together. However, longer base-line observations introduce their own systematic errors, complicating accurate measurements of both the physical properties and their confidence intervals.

This work analyzes a low quality lightcurve of the near earth multiple system 2577 Litva. We use this object to highlight various techniques for working with lightcurves of this nature, performing high quality measurements on data with a low signal-to-noise ratio. Section 5 describes our observations and the archival data used as well as the history of the multiple system 2577 Litva. We then present robust statistical methodologies for analyzing low signal-to-noise observations as well as generating accurate uncertainty estimates in section 5. Finally, in section 5, we apply our routines and present the analysis of Litva comparing our results with previously published works. In addition, we present physical properties, such as the direction of the rotation axis (pole direction), determined in the course of accounting for rotation systematics. This work demonstraits the validity of this methodology with a high signal-to-noise object, and providing confidence for use in future low signal-to-noise analysis.

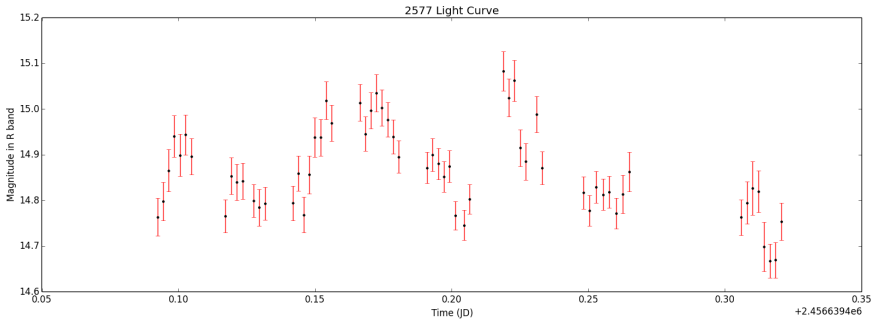

Figure 5.1: Observations of 2577 Litva from Robinson Observatory over the course of one observing night

Observations and Background

2577 Litva is a Mars-crossing asteroid discovered in 1975 by N. Chernykh. In 2009 the object was determined to be a binary member of the Hungaria family (Warner et al., 2009b). As a binary, the object warranted aditional follow up as there are relatively few binaries known and opportunities to determine physical properties are extremely valuable. Merline et al. (2013) discovered a second satellite orbiting Litva with observations in June and August 2012, as well as August and October 2013.

The data used in our study was a mixture of new observations and reanalysis of existing archival data sets. The newly collected data provides us with fresh sampling of the body, in an environment where we were able to control and understand the entire collection process from observation to reduction. The archival data helped with comparisons to previously published figures, and in identifying the presence of eclipsing events (either parent on satellite or satellite on parent, known as a primary or secondary eclipse).

Additional observations of Litva were taken from Robinson Observatory located at the University of Central Florida. The observatory features a 0.5 meter Ritchey-Chretien telescope on a MI-750 German equatorial mount. The imager is a SBIG 6303e CCD camera with a 0.46 arc-second plate scale. The data was recorded over the course of several weeks spanning from December 2013 through February 2014. We used exposure times of 2 minutes and 30 seconds to balance signal-to-noise requirements against time resolution in the observations. Each observation represented integrating over approximately 1.5% of the primary rotation period. In total we acquired 520 usable observations, which were analyzed using aperture photometry and techniques laid out in Lust et al. (2011). The result was a brightness time series known as a lightcurve. A portion of the lightcurve covering one nights observation is shown in Figure 5.1.

Archival data for Litva was obtained using the asteroid lightcurve database (Warner et al., 2009a). We used data obtained by B. Warner,D. Higgins, C Bembrick,and R.D. Stephens, from March 2009, July 2010, and August 2010. Additional data from April 2012 taken by J.W. Brinsfield was used as a control to verify our results, but was not used in the modeling and reduction process. We used the raw data from the archive but performed our own calibrations.

Methodology

We present the routines used to analyze our data in two parts. Section 5 presents methodologies for determining physical properties through Bayesian investigation outlined in Gregory (1999). In this section we introduce modifications for dealing with differing observational view points arising from the mutual orbits of Earth and the body being investigated. Section 5 describes how corrections to orbital systematics are made, and how this leads to the determination of the pole direction. These methods allow meaningful measurements along with error estimates to be made for a number of physical properties, providing a more comprehensive picture of Litva, and by extension asteroids in general.

Bayesian Inference of Asteroid Properties

The lightcurve of an asteroid, generated by reflected sunlight off the rotating body, encodes physical properties such as rotation period,shape, major morphological features, or presence of a satellite. Determining these physical properties involves fitting mathematical models to the measured data. Harris & Lupishko (1989) outlines the most frequently used model, based around a Fourier series of sine waves. The parameters of this model are the amplitudes and phase of each component sine wave, and the period of rotation. A second method, Stellingwerf (1978), involves mapping

each time value to a percentage through one rotational period (know as the phase) of the body. The data is binned and the variance in each bin is computed and summed. The period is varied until the variance is minimized, giving this technique the name phase dispersion minimization. Both methods use a function which attempts to optimize parameters such that once the model is removed, the variance of the residuals is minimized. These minimizer functions work by following gradients in parameter space to arrive at a minimum. Each of these methods has their own advantages and disadvantages, and covers enough material to be the subject of an entire paper separately.

Gregory (1999) outlines a different model, originally developed for analyzing lightcurves from rotating stars. This routine shares some features with the standard methods, but uses Bayesian statistics to explore the parameter space in place of a minimizer.

Before continuing with the application of Bayesian inference we will briefly outline how the process works. Equation 5.1 is the Bayes theorem and is the core of all Bayesian inference. This theorem states that the probability of a given parameter θ given a model M and data D ($P(\theta|M,D)$,known as the posterior probability) is equal to the probability of the parameter given the model ($P(\theta|M)$) times the probability of the data given the parameter and model ($P(D|\theta,M)$) normalized by the probability of the data given the model integrated over all possible parameters ($P(D|M)$). The quantity $P(\theta|M)$ is known as the prior distribution of the parameter. If it is known that the parameter falls according to some distribution, say a normal distribution, the probabilities are weighted by this distribution. If no prior information is known about the parameter, an uninformative prior may be used, typically some form of uniform distribution which may or may not span all of the parameter space. An uninformative prior with limited parameter space may be thought of as a step function, all values in a range are given equal weighting, but outside the range the weight (likelyhood) is set to zero. This reflects prior knowledge that the parameter cannot be above or

below certain values, perhaps from physical arguments, but what value it takes on inside the range is unknown. The normalization term $P(D|M)$ can be thought of as the average probability of the data given the model, irregardless of what parameter is chosen. Often times in Bayesian inference the absolute probability of a parameter is not as important as the relative probabilities between parameter values, and the normalization constant is excluded from the calculations.

$$P(\theta|D, M) = \frac{P(\theta|M)P(D|\theta, M)}{P(D|M)} \tag{5.1}$$

Bayesian inference is well suited for working with data collected in real world scenarios. Every part of the inference, from the data, to the results are treated as probability distributions. This makes it especially well suited for dealing with low signal-to-noise data sets, as well as generating meaningful uncertainty estimates with proper uncertainty propagation though each step of the analysis. Another useful feature arises with how the method is able to deal with unknown, unconstrained, or otherwise uninteresting parameters. When outlining the theorem, we have used θ as a single variable in the model M, but it need not be a single variable, and can represent a vector of variables. In such a case the only modification is that the prior probability function $P(\theta|M)$ is replaced by a multiplication of the prior probability distribution for each parameter. If only one parameter in the model is of interest, integrating over the range of possible values for each of the other variables will suitably take them into account in the distribution function of the parameter of interest. This is known as marginalizing over a parameter (or many parameters). An example of this would be marginalizing over a parameter representing the dimming of a lightcurve with distance from the sun when generating the distribution function representing the period of the lightcurve.

Another benefit of Bayesian inference arises from the structure of the theorem itself. If the investigation can be explicitly written out in analytical form it is possible to do many calculations 'pen and paper' style and find a functional representation of a parameters distribution without the need for a computer. Though this is not possible when a parameter is implicit, rather than explicit in an expression, it is sometimes still possible to marginalize certain parameter into a simplified expression before investigation with a computer. This can sometimes greatly reduce the computation time necessary for generating the posterior distribution of a parameter. Finally we will highlight how with Bayesian inference the model itself can be thought of as a parameter, which can be useful for assessing the probabilities that various models accurately represent the data. An example of this could be comparing a linear vs. quadratic fit for the bias levels in a charge-coupled device (CCD) camera.

$$j(t) = int[1 + m[(\omega t + \phi) mod 2\pi]/(2\pi)] \tag{5.2}$$

$$\begin{aligned} p(D|\omega, b, \phi, M_m) =& (2\pi)^{-\frac{N}{2}} (\Delta r)^{-m} [\prod_{i=1}^{N} (s_i)^{-1}] (\frac{\pi}{2})^{\frac{m}{2}} b^{\frac{N-m}{2}} exp(\frac{-b}{2} \sum_{j=1}^{m} \chi^2_{W_j}) \times \\ & \prod_{j=1}^{m} [W_j^{-1/2} [erfc(y_{j_{min}}) - erfc(y_{j_{max}})]] \end{aligned} \tag{5.3}$$

$$\chi^2_{W_j} = \sum_{i=1}^{n_j} \frac{(d_i - \overline{d_{W_J}})^2)}{s_i^2} \tag{5.4}$$

$$W_j = \sum_{i=1}^{n_j} \frac{1}{s_i^2} \tag{5.5}$$

$$y_{j_{min}} = \sqrt{\frac{bW_j}{2}}(r_{min} - \overline{d_{W_j}}), y_{j_{max}} = \sqrt{\frac{bW_j}{2}}(r_{max} - \overline{d_{W_j}}) \tag{5.6}$$

$$p(b|M_m) = \frac{1}{bln(b_{hi}/b_{lo})} \tag{5.7}$$

$$p(\omega|M_m) = \frac{1}{\omega ln(\omega_{hi}/\omega_{lo})} \tag{5.8}$$

The model used by Gregory (1999) to represent lightcurves is a piece-wise step function, similar to what is used in phase dispersion minimization. With this, the lightcurve is approximated by a constant value in each phase bin. By varying the number of bins m we get a class of models that is highly adaptable, and able to model complex arbitrary shapes. In order to compare this model with lightcurve, each of the times corresponding to a data point must be mapped to its corresponding phase value according to equation 5.2 where ω is the lightcurve's angular frequency, t is the time index, and ϕ is the over all phase shift between different nights. If all data are referenced from the same time value then ϕ is zero. In order to use Bayes' theorem, we use the expression presented in equation 5.3, but leave the derivation to Gregory (1999). Equation 5.3 represents the probability of having data D given the various parameters. As the shape of the lightcurve is unknown, distribution function has already been marginalized over the shape parameters r_j. In this equation m gives the number of bins in the piece-wise step function, N is the total number of data points, s_i is the uncertainty associated with each data point, b is a scaling factor (if the uncertainty on the data points is over or under estimated as determined by the maximum likelyhood of a Bayesian

inference) often it is set to 1 indicating uncertainties are not to be scaled, $\chi^2_{W_j}$ is given in equation 5.4 and describes how well the piece-wise function fits a particular bin j. W_j is given in equation 5.5 and is the sum of one over the uncertainty squared for all the data points inside a particular bin j. Finally $y_{j_{min}}$ and $y_{j_{max}}$ are given in 5.6 and are related to how each bin j corresponds to the marginalized shape parameters r.

To use Bayes' theorem for investigating each of the model parameters we also need to assign prior distributions to them. It would be possible to use uniform distributions over some range, however we adopt the priors from Gregory (1999) as they have been shown to better describe the unknown behavior of the variables, with the exclusion of ϕ as we tie all our data to a common origin and thus ϕ is equal to zero. Equations 5.7 and 5.8 outline the established priors. With these it is possible generate probability distributions for each parameter by marginalizing over each of the others. We make note that to speed up some calculations it is possible to find optimal values for some parameters, such as b, and substitute the most likely value in all subsequent investigations without having much impact on the subsequent distribution.

The Bayesian framework of Gregory (1999) also provides a method for generating a model of the shape of the asteroid. Using the most likely period, determined from the model marginalized over the shape parameter, a series of piece wise step functions can be generated. At a particular number of bins m the value of the model at each time t is the average of each of the data-points in the same bin as time t. Different values of m will produce different binning, and thus different values for each t. Each of these differing models can then be averaged with equal weighting to produce a model smoother than the initial step function. Alternatively the same Bayesian inference process can be used to generate a probability distribution function for the likelyhood that each value m best represents the data. This distribution function may then be used as weights in the inter-model averaging process.

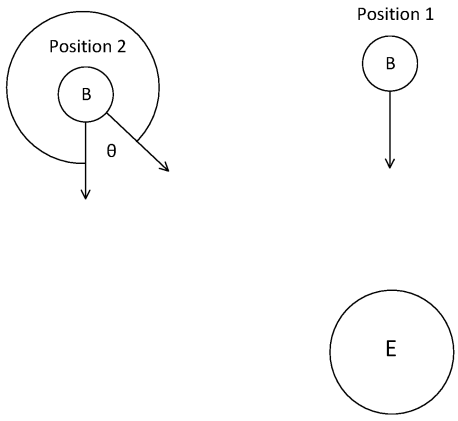

Figure 5.2: A cartoon demonstrating the effects of orbit on determining periodicities.

Through Bayesian inference we now have a framework to determine the probability distribution function for parameters, such as period, of the model outlined by Gregory (1999). This model, however, is not completely sufficient for investigating asteroid lightcurves as it was designed for working with stellar sources. These objects are sufficiently far away such that through the course of the Earth's orbit the viewing geometry of the system does not change appreciably. This is not the case when observing solar system objects, as the mutual orbits of the Earth and the body under observation lead to differing vantage points of observation.

To understand why the orbit of a body will affect the measurement of a period we remind the reader of the difference between a sidereal and solar day. A sidereal day is measured by picking the location of distant stars in the sky as a reference point, and then measuring the time elapsed until the same stars get to the same position in the sky. When measuring a solar day, the position of the sun in the sky is used as a reference. The day is then the time elapsed between the sun starting at a particular place, say directly overhead, and returning to it. Because the Earth is orbiting as

well as rotating, after a 360 degree Earth rotation the sun will not be directly over head, and Earth must rotate a bit more for it to return to that location. This is because of the distance moved in the Earth's orbit around the sun during one day. In contrast, a sidereal day is where the a distant star will appear back in the same position after only 360 degrees, as the parallax of the distant star due to the Earth's orbit is so small.

Observations of orbiting asteroids exhibit a very similar phenomia, depicted with a cartoon in Figure 5.2. In this figure E represents Earth, and B is the body being observed. In position one a particular feature, denoted by the arrow, is pointing along a direction toward Earth. This feature is represented in the lightcurve, a maximum or minimum of flux, but can be at any point in the rotation of the body. If the position of body B did not change, then after it had rotated through 360 degrees the feature would again point in a line directly towards Earth. However, because body B is orbiting about the sun, its position does change, as denoted by position two. Body B was rotating at the same time as it was orbiting, and thus after a 360 degree rotation the feature denoted by the arrow is now parallel to it self in position one, but is not pointing towards Earth and must rotate through some angle theta before it is seen as in position one. Because the rotation rate of the object is constant the extra rotation through theta will be observed as the feature showing up later in the time series than it would if the body was not rotating. If the senses of rotation were different, or the Earth's position were to lead, the only difference would be the sign of the additional angle.

These angular corrections are analogous to the phase parameter initially discussed with the model, except there will be a phasing parameter associated with each observation. As will be layed out in section 5, this phasing parameter will not only depend on the relative position of Earth and the body (parameterized by the observing time t) but also by the direction of the asteroid's rotation axis. Equation 5.9 is a modification of the function which determines which phase bin each data point belongs in. We introduce the term $\psi(t, \lambda, \beta)$ which is the parameterized representation of the orbital effects on the observational phase of the body. The negative sign in the equation represents

the convention for correction we have adopted. Unless the body being observed is near to the Earth and moving rapidly, phase corrections over short time scales will all be very close in value. With low signal-to-noise data-sets the variance may be larger than the phasing effect, in which case it may only be possible to constrain which values are excluded vs which values are likely to be correct. In these cases, or when only period information is desired, these angular corrections can be marginalized such that the uncertainties of the other parameters better reflect the uncertainties of the measurements. By not taking this correction into account, even over short time spans, the phase effect will cause dispersion in the measurements which will resemble a higher noise level. This may lead to incorrectly determining the period, as standard minimization routines will attempt to balance the scatter in the data around the tested model. Because the uncertainties reported with these techniques are often the formal errors from the model fitting, they will not encompass the possibilities that the model is not fully representative of the data. The results of our period analysis, section 5, are presented with this marginalization and corresponding uncertainty limits. A full analysis as well as additional results can also be found in section 5.

$$j(t) = int[1 + m[(\omega t + \phi - \psi(t, \lambda, \beta))mod2\pi]/(2\pi)] \tag{5.9}$$

Orbital Timing Correction

The problem of orbital phase corrections is more complicated than the simple cartoon of Figure 5.2. In reality the Earth is also in orbit about the sun, and the orbital planes of Earth and the body are most likely inclined with respect to each other. The Earth's orbital position will introduce a further complication into determining the extra rotation angle of the body, as shown in figure 5.3. In this depiction the Earth is interior to the object and thus progresses through its orbit faster. The inclination effect will manifest as a changing amplitude in the lightcurve. If the observations are

taken close enough in time, and the body is not unreasonably close or have a pole direction near parallel with Earth's orbital plain, the changing amplitude will be below the level of uncertainty in the lightcurve brightness measurements and can be ignored. Alternatively, if the period determination routines being used only take into account relative amplitudes the inclination effect will not matter. For the matter of rotational timing we only need to consider the positional effects of the bodies.

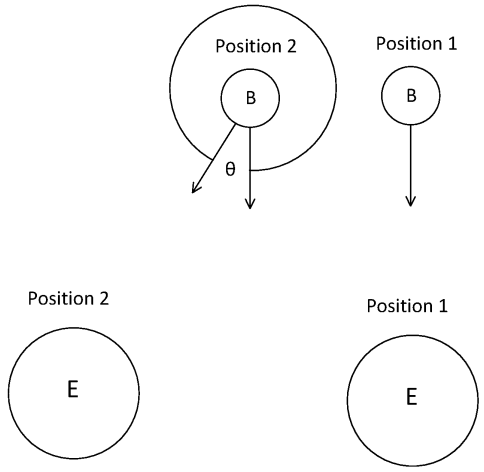

Figure 5.3: A more detailed cartoon depicting the mutual orbits of the body and Earth.

Firstly the three dimensional heliocentric Cartesian vector coordinates for both the body and the Earth must be obtained corresponding to each observation. For this we use the horizons[1] tool provided through JPL, but any tool that produces this information will work equally as well. By subtracting the vector for the body, in our case Litva, from that of Earth, the coordinate system is transformed from a Sun centered into a body centered reference frame. In this system each vector is now one which points from the center of the body towards the center of Earth at the time of each observation.

[1] http://ssd.jpl.nasa.gov/?horizons

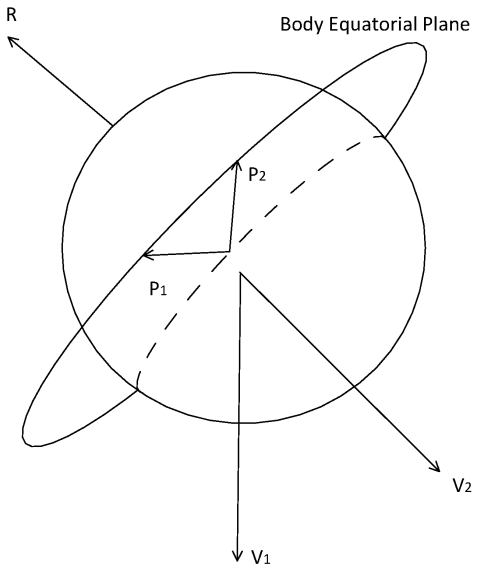

Figure 5.4: Body-Earth vectors depicted in body centeric coordinates

If the Earth and body were in the simple arrangement shown in Figure 5.2, finding the extra angle the body must rotate though between two observations would be as simple as taking the dot product between the vector corresponding to the first observation and the vector for each subsequent observation. However, as indicated above, the solution is not that straightforward. Figure 5.4 depicts the arrangement in our transformed body-centeric frame. By switching coordinates the mutual orbits of both the body and the Earth are taken into account by the direction of the vectors pointing towards the Earth, two positions of which are depicted by V_1 and V_2. For further illustration Figure 5.5 depicts the vector end points pointing towards the earth centered on 2577 Litva. We make note of the curved shape, with motion in each dimension.

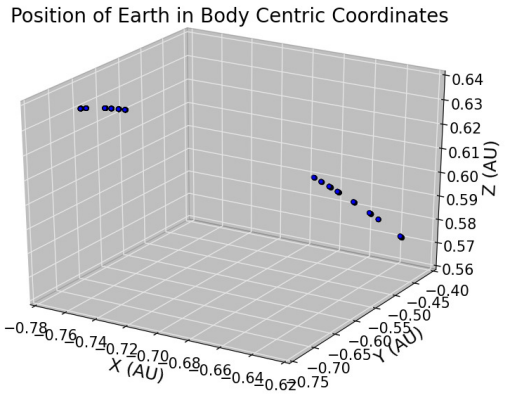

Figure 5.5: Position of Earth as seen by Litva in body centric coordinates.

Our solution to the orbital phasing problem will seem familiar to those who work with light curve inversion. Specifically it bears resemblance to pole determination routines of Drummond et al. (1988). When determining the extra rotational angle of the body, we are only concerned about the components of these vectors which lay in the direction of rotation, and thus we must first define the axis about which the body rotates. The pole direction is defined by the two angular components of the spherical coordinate system, θ and ϕ. In the context of astronomy these angles are taken to correspond to the direction the pole points to in latitude and longitude in the ecliptic coordinate system. With these angles and a unit radius we can define a new Cartesian vector along the pole direction, which is perpendicular to, and defines, the body's equatorial plane. The body-Earth vectors, again depicted by V_1 and V_2, must then be projected onto the equatorial plane, depicted by P_1 and P_2. The angle between each projected vector and the vector corresponding with the first observation will be the extra rotation the body must go through for each object to match the aspect of the first observation.

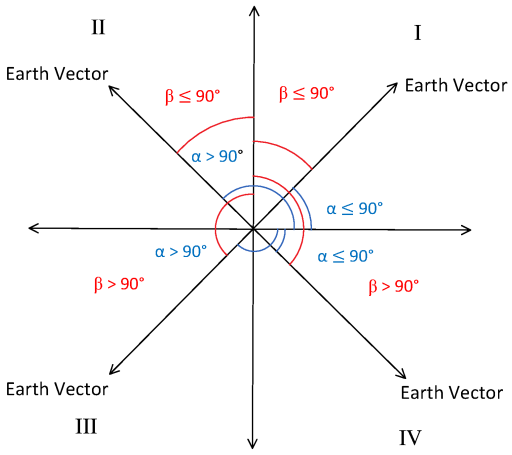

Figure 5.6: Depiction of reference plane and Earth vector, demonstrating which quadrants correspond to what angles formed with the x and y axes.

One final consideration is the direction of the angular change, i.e. is a particular feature phased such that it appears to arrive early or late as shown in figure 5.3. To determine this, we construct yet another reference frame centered on the body with the pole direction as our z-direction. The vector defining the x-direction may be any vector perpendicular to the z-direction, but it makes sense to use the projected vector corresponding to the first observation as it allows for a simple time stepping through subsequent observations. Additionally because the vector has been projected into the observation plane we know it is perpendicular to the z-direction, as the projection plane is defined to be perpendicular to the pole direction. Finally we cross the x and z directions to define a new y-direction.

With the x and y vectors defined as directions in the body's equatorial plane we now have a system that is analogous to the quadrant system familiar from algebra, shown in in Figure 5.6. We define two angles, α and β, as the dot product between any particular projected Earth vector and the x and y axes respectively. We take a moment to note that an astute reader will notice that since we defined our x-axis as our first observation direction projected onto the equatorial plane, the angle

α corresponds with the time phasing angle in the rotational period. Returning to Figure 5.6 we can see that if a subsequent observation has a corresponding vector which lays in quadrants I or II, then we would expect a given feature to "show up late" and have a positive phase delay. If the vector lays in quadrants III or IV this would represent a feature arriving early and would have a negative phase delay. Determining which quadrant any given vector lays in can be done by investigating α and β as shown in the figure, and in Table 5.1. It is important to note that this directionality of sign is based on the body rotating prograde. If the sense of rotation is retrograde then these signs will be reversed. By analyzing which sign produces the lowest residuals, the directionality of rotation can be determined.

Because of how we define the coordinate system it does not matter which body is closer to the Sun. Figure 5.3 shows that as the Earth orbits faster, vectors in the third quadrant (as defined by a reference vector pointing in the general direction of the sun) will become negative, as the feature appears to arrive early. If the body was instead inside Earth's orbit, it would instead orbit faster, however the initial reference vector (pointing from the body towards Earth) would be pointing generally away from the sun. Thus, in this the third quadrant of our reference frame would still represent a given feature appearing early.

Table 5.1: Table showing which combinations α and β angles correspond with what quadrants

Quadrant	α	β
I	$\alpha \leq 90°$	$\beta \leq 90°$
II	$\alpha > 90°$	$\beta \leq 90°$
III	$\alpha > 90°$	$\beta > 90°$
IV	$\alpha \leq 90°$	$\beta > 90°$

With this methodology we can correct a lightcurve for the delay or advancement in timing due to orbital effects given the positions of the Earth and the body, along with the pole direction. As noted the directions of the body can be determined by any orbital integrator, for which we use JPL's Horizons, which leaves the determination of the pole direction. For this we again rely on Bayesian inference to determine the probability distribution of the pole parameter. Like before, this is proportional to the prior likelyhood of the pole direction times the likelyhood that our data is consistent with the value of these parameters. For the prior likelyhoods, as we do not already know the pole direction, we take uniform distributions over $0, \frac{\pi}{2}$ in latitude, and $0, 2\pi$ in longitude. To determine the likelyhood that our data corresponds to given parameter values, these values are used to generate a model of the data according to the phases given by equation 5.9. Because these two parameters greatly expand the phase space that must be searched, we use a Bayesian inference methodology of ter Braak & Vrugt (2008). Their routine uses a specialized Monte Carlo (random stepping) style approach to intelligently search the phase space. This is faster than explicitly generating the entire joint distribution, and has been shown to converge to the analytical distribution as the number of steps in the Monte Carlo gets large. Additionally, our specialized implementation has been shown to converge much more rapidly than traditional approaches, and is able to deal with correlated parameters by moving along the direction of mutual co-variance.

Determining the pole direction, and correcting the phasing effects of the orbit in the mannor we have described is dependent on the strength of the dispersion due to the orbital effects. To make meaningful measurements of this effect, it must be greater than the noise level of the observation. If this criteria is not met, it may still be possible to exclude certain values of phase space, but not precisely determine which values are most likely. This either requires moderate to high signal-to-noise data, or many data-points. The greater the distance through the orbit the greater the dispersive effect. In an ideal situation if there is a good estimate of the period of rotation, the orbital span required at a particular signal-to-noise could be estimated for a range of pole directions

and observations planned accordingly. If suficient observations can't be done in a semi contiguous manor (over a short time frame), then the period uncertantly becomes increasingly a problem as there is no way to know exactly how many rotations the body has undergone. The uncertainty makes it difficult to tell if the phase change observed is due to orbital phasing effects or rotational effects. A one second uncertainty in period on each revolution of the body over months to years leads to a situation where the phase that the body "should" be in is impossible to predict. In these conditions more orbital positions spaced over the orbit are required to disentangle the effects of orbit vs rotational uncertainty and narrow down the probable values in phase space. When observational brightness and telescope facilities are available, a frequent observing schedule should make it possible to determine the probable pole direction over a relatively short time scale.

Results

The methodology outlined in section 5 was used to analyze the our data (section 5). We sought to identify and characterize the primary rotation period, an additional rotation period present in the data, the presence of an eclipse from the companion object, and the pole direction of the primary. Extensive effort was put in to properly quantify the uncertainties in addition to the most likely value.

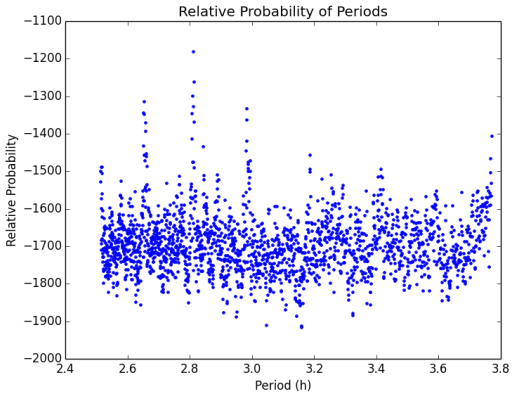

Figure 5.7: Relative probabilities of periods over the suspect range.

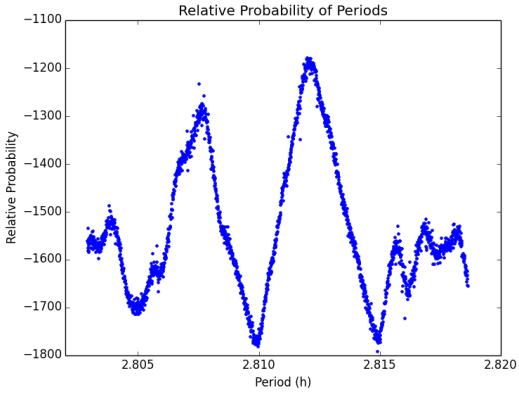

Figure 5.8: Relative probabilities over a range near the most probable value.

Primary Rotation Period

Visual inspection of our collected lightcurve (5.1) leads to the conclusion the rotation period of the primary lies between 2.5 and 3.5 hours. Figure 5.7 depicts the relative probabilities in logarithmic scaling for each of the periods in the range to be investigated. The most probable period appears to occur near 2.8 hours, we therefore do a more detailed analysis in that range shown in figure 5.8. From this we determine a most probable period of $2.81209 \pm 0.0018h$ comparable to $2.81258 \pm$

$0.00002h$ reported in Warner et al. (2009b). Though these two values only differ by about 2.5 seconds, the error bars of the two measurements do not overlap at the one sigma level. At the three sigma level our measurements do encompass their value, but the converse is not true. We make note that our error bars do appear to be an order of magnitude larger, but this is due to inclusion of, and marginalization over, the uncertainty distribution of the pole direction. Because this effect is not taken into account, the fitting of the original measurement may have been skewed towards the larger period with the formal error bars of the least squares fitting not encompassing the full uncertainty. Figure 5.9 depicts our observations phased around the most likely period, as well as the model for the lightcuve.

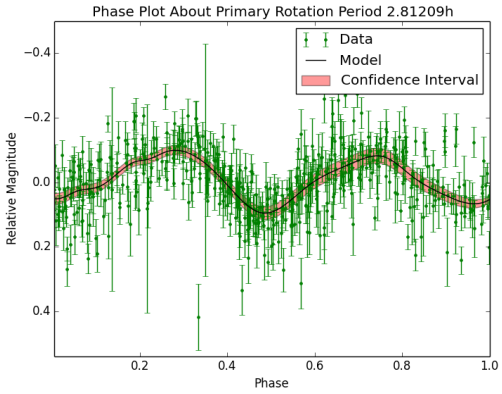

Figure 5.9: Our Litva observations phased around the most likely period along with a model of the lightcuve shape.

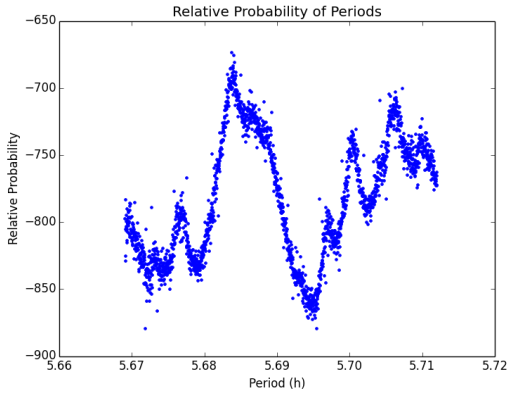

Figure 5.10: Relative probabilities of periods in a large region around the additional rotation period.

Additional Rotation Period

Warner et al. (2009b) reported discovering an additional rotation period present in the data after the primary rotation period was removed. They suggested that this was the rotational period of a third satellite in the Litva system. This was expanded upon by Pravec et al. (2012) who discovered this additional rotational period was still present even when the secondary object was in eclipse. To analyze this period we subtract the model shown in figure 5.9 from our data set leaving the residual signal. Since we have an idea of the period from previous works we search in the area near the published value akin to searching for the primary signal. This is not as clearly defined as the secondary signal is weaker, and we get a few signals which are a confluence of random noise which lead to a strong uniform model. After testing each peak we identify the secondary signal as shown in figure 5.10. We identify the most likely period for the additional signal to be $5.68389 \pm 0.0005h$. This value is comparable to the published value of 5.6842 ± 0.00002 in that our

error-bars just about encompass the published value at the one sigma level. The two measurements differ by about a second, with ours slightly shorter in duration. We again attribute the differences in value to the uncertainty accounting. Figure 5.11 shows our data phased about the most likely period. We choose to leave out the error bars on this plot, as the amplitude of rotation is near the level of error on a per data-point bases which makes the plot cluttered on visual inspection.

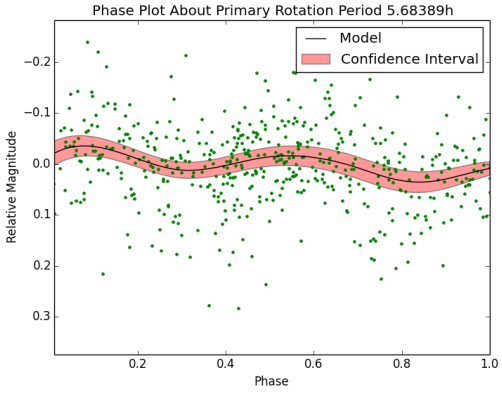

Figure 5.11: Phase plot of the additional rotational period around the most likely value

Binary Eclipse

In a binary system the presence of eclipses (either primary or secondary) is of interest, as it aids in the determination of orbital period, size ratios of the components, and mass of the system. Warner et al. (2009b) first detected these eclipses and provides constraints on the relative timing between events, duration of events, as well as the orbital period. Figures 5.12 and 5.13 show our data phased about the published orbital period of $35.81h$. The top figure is the data phased containing the rotation periods of the components, while the bottom has those periods removed. In either plot we see no strong eclipse present. There may be a hint of an eclipse near 0.32 and 0.81, but the level is not much above that of the noise, and certainly not as deep as those observed in Warner et al. (2009b).

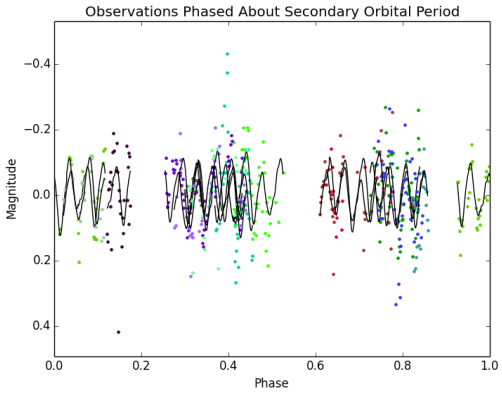

Figure 5.12: Observations of Litva phased around the secondary orbital period including the rotation periods of the system.

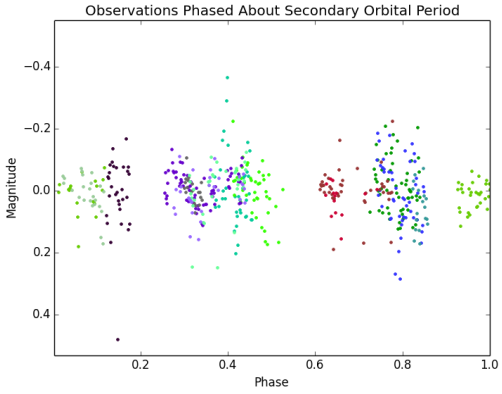

Figure 5.13: Observations of Litva phased with the rotation periods removed.

The lack of a prominent eclipse could mean one of two things; (1) from Earth's vantage point there is no, or a very weak, eclipse or (2) the eclipse happened at a cadence such that our observations missed it. To be sure of possibility one, we must rule out the second possibility. We do this by assuming that the eclipse must have occurred at some point in the preceding 1.49 days (one orbital period) before our first observation. We then create test points which span every 15 minutes for one orbital period. These test points represent the times at which the center point of the hypothetical

eclipse occurs. Each test point is then propagated forward in time at the period of the satellites orbit. The propagated test points are compared to the times of each of our observations. If any of the propagated test points falls within 15 min of one of our data points we say that an eclipse at that test position would have been detected We do this looping over each test point. We are further aided that in a given orbit there would be two phase positions which would have been dimmed by mutual events between the primary and secondary objects. For detection we don't care which object is the one eclipsed, only that a deviation from the standard brightness occurred, we can test our propagation at half the orbital period, increasing the odds that we would have successfully detected an event.

Our analysis only finds two locations that are not within 15 minutes of an observed data-points. Each of these are within 30 minutes of a data-point, which is within the eclipse window determined by Warner et al. (2009b). This indicates that unless the geometry of the Earth/body is such that the mutual events occurred over a short time frame (i.e. a glancing detection short in duration and or with an amplitude comparable to our noise level) we would have been able to detect it.

Though no detection is evident in our data this null result is none the less useful. When trying to model the orbital plane (defined by the pole direction of the orbit) it is as important to know what vantage points do not show an eclipse as it is which ones do. By comparing various vantage points and the visibility of the secondary object one can invert what pole direction is necessary to give these results.

Primary Pole Direction

When applying our methodology for determining pole direction we determined our data was not of sufficient duration (covering enough orbital distance) to produce a phase dispersion larger than the variance of our data. Because of this, we used archival data as mentioned in section 5. We used three data-sets for the modeling (ours and two from Warner et al.), and one as a control to test the effects of the determined pole against the data used in the modeling.

Including the archival data in our analysis increases the total time span of observations to about five years. As we discussed in section 5 period uncertainties over this range of time make it impossible to know now many rotations the body has undergone, and thus what phase the body should be in. This produces strong correlations between the parameters of period and those of the pole direction. We therefore use our Bayesian inference to explore the joint distribution of the period along side the latitude and longitude of the pole. Because we have an estimate on the period and associated errors of the body, we can use this to construct a prior likelyhood to reduce the possible phase space of the period and speed up computations. For completeness we take the prior range on the period to be three times that of our determined errorbars on the parameter. The latitude parameter is allowed to vary over $0, 90$ degrees, while longitude varied from $0, 360$ degrees.

Because it is not possible to easily plot out the three dimensional probability distribution we will instead present the data as several two dimensional histograms. For the initial inference figure 5.14 shows the joint distribution of period with latitude, figure 5.15 shows period with longitude, and figure 5.16 shows latitude with longitude. The first thing which is evident is that there appears to be three distinct regions of interest. This is more clearly seen in figure which depicts the probability distribution of just the period. These figures indicate that there are three regions in which the parameters give a high probability of corresponding to our observed data.

For further investigation of the three regions of interest in figures 5.14, 5.15, and 5.16 we isolate a single period by placing a more restrictive prior likelyhood at the peak near 2.8125 and generating the corresponding joint distribution. We then take the most likely parameters and assess the performance of the routine by creating an orbit corrected phase diagram for each of the data-sets, as seen in figure 5.18. It is clear why this is a high probability combination of parameters, as peaks line up with peaks, and troughs line up with toughs. However, as lightcurves are bi-modal (they typically have two defined peaks) we can see that with this combination of parameters the wrong peaks are aligning, making this combination incorrect. This is further evident when we include the phase diagram of our control curve (data from J.W. Brinsfield), figure 5.19. Similarly we investigate the period near 2.8128 hours as shown in figure 5.20. With this set of parameters it appears there is good agreement with the lightcuves, but when we include the control, figure 5.21, we can see this set of parameters is also excluded.

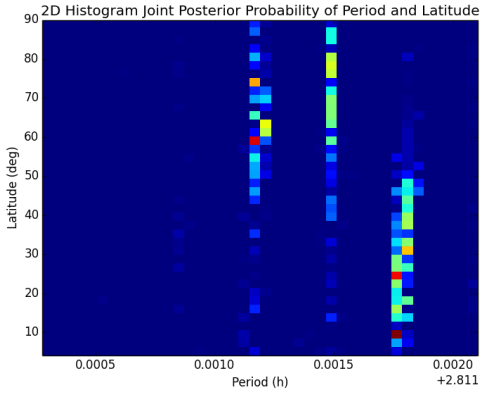

Figure 5.14: Joint probability distribution of period and latitude parameters for the global inference

When we investigate the period centered near 2.8122, however, we can see good agreement between the data-sets used for modeling (figure 5.22) as well as with the control data-set (figure 5.23). We can thus conclude the joint distribution including the 2.8122h period has the highest likelyhood of correctly modeling the system and represents the true period, latitude, and longitude. Figures 5.24 - 5.26 show the joint distributions for the correct parameters, while 5.27 - 5.29 show the individual distributions. We find the most likely prameters to be, a period of $2.812186 \pm 5x10^{-6}$, latitude of 62.96 ± 2, and longitude of 292.8 ± 11. For completeness we tested the same procedure for retrograde rotation but did not find any combination of parameters which worked.

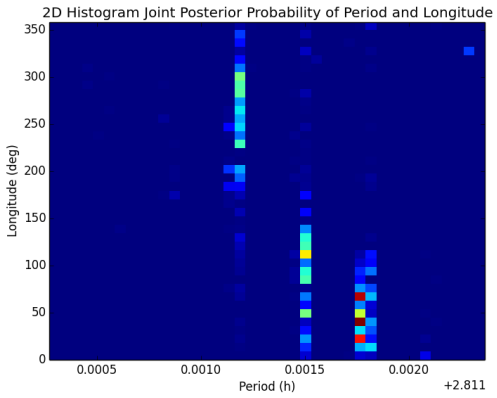

Figure 5.15: Joint probability distribution of period and longitude parameters for the global inference

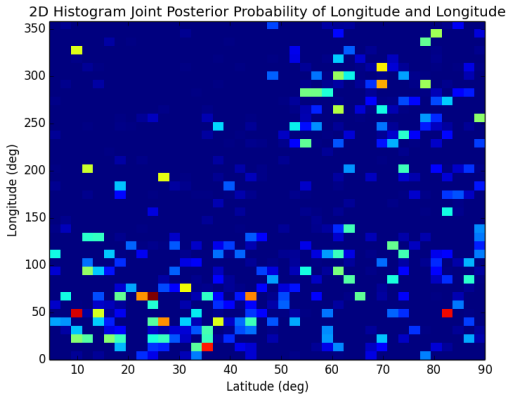

Figure 5.16: Joint probability distribution of latitude and longitude parameters for the global inference

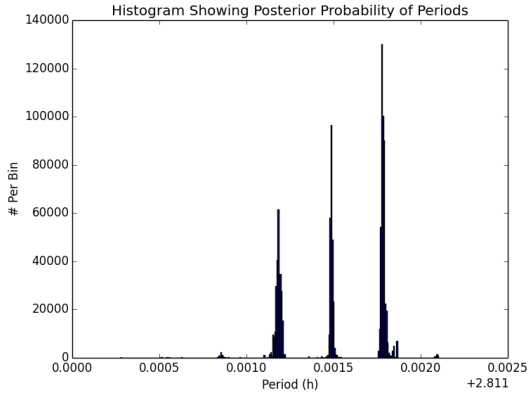

Figure 5.17: Probability distribution for the period parameter of the global inference. Note to show fine detail the scale on the period axis starts at 2.811h

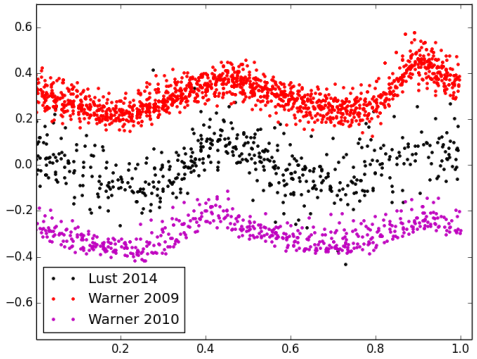

Figure 5.18: Phase plots corrected for orbital effects using the joint probability distribution including a period of 2.8125h

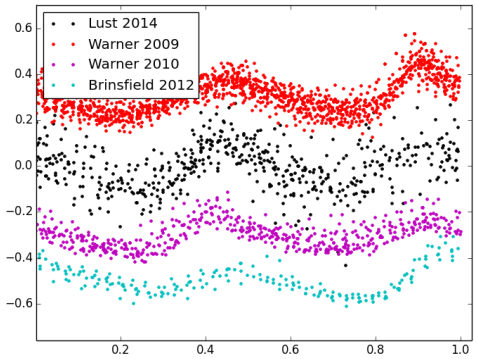

Figure 5.19: Phase plots with the control corrected for orbital effects using the joint probability distribution including a period of 2.8125h

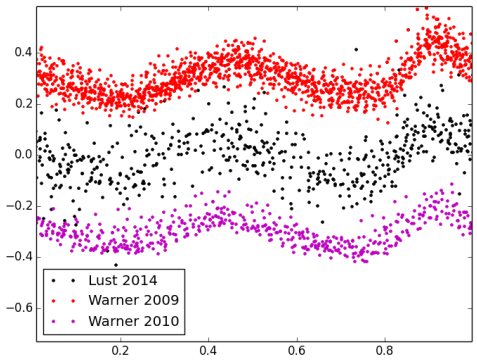

Figure 5.20: Phase plots corrected for orbital effects using the joint probability distribution including a period of 2.8128h

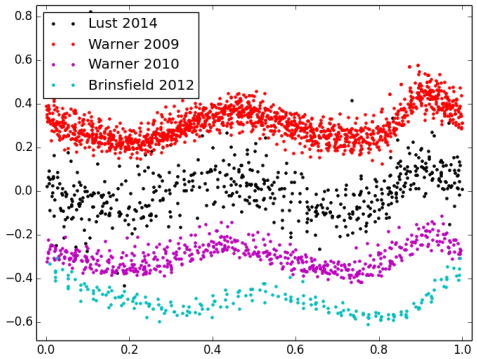

Figure 5.21: Phase plots with the control corrected for orbital effects using the joint probability distribution including a period of 2.8128h

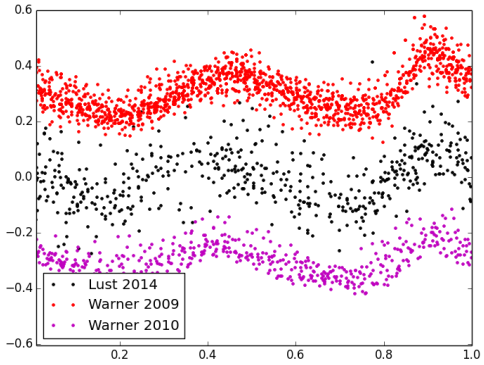

Figure 5.22: Phase plots corrected for orbital effects using the joint probability distribution including a period of 2.8122h

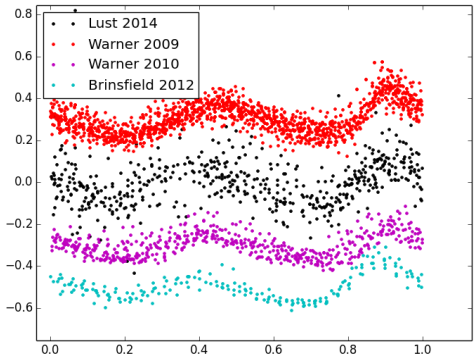

Figure 5.23: Phase plots with the control corrected for orbital effects using the joint probability distribution including a period of 2.8122h

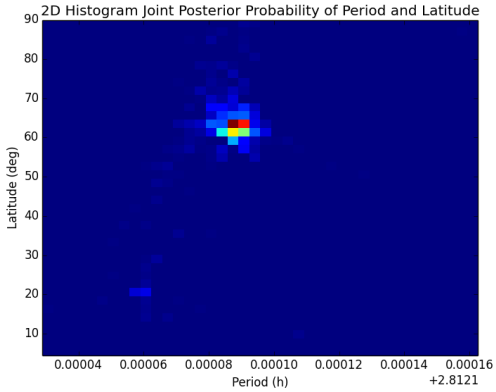

Figure 5.24: Joint probability distribution of period and latitude for the correct parameters

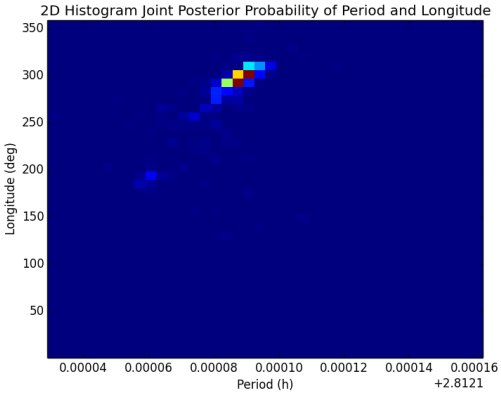

Figure 5.25: Joint probability distribution of period and longitude for the correct parameters

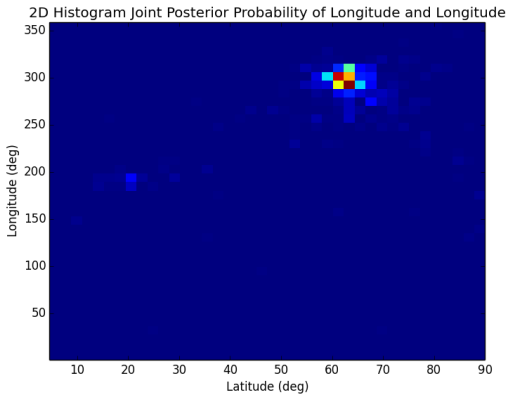

Figure 5.26: Joint probability distribution of latitude and longitude for the correct parameters

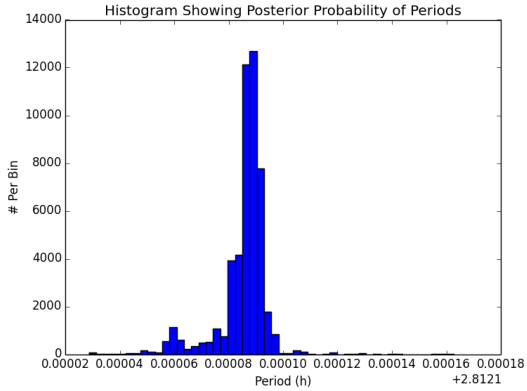

Figure 5.27: Probability distribution for the most likely period. Note the scale on the period axis starts at 2.8121 to better show fine detail.

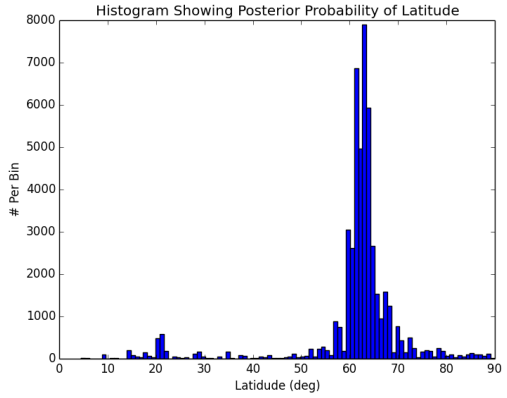

Figure 5.28: Probability distribution for the most likely latitude

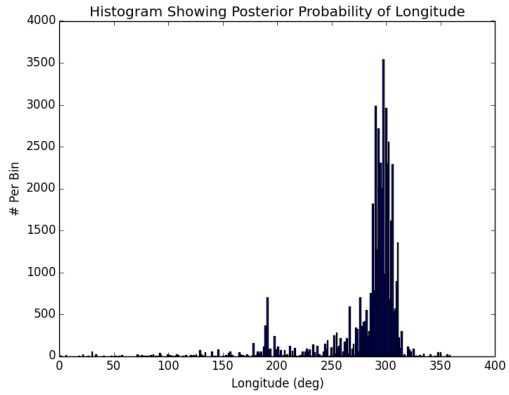

Figure 5.29: Probability distribution for the most likely longitude

Conclustions and Future Work

In this work we have shown how Bayesian inference is both competent and useful for precise modeling of asteroid lightcurves and determination of their properties. A major advantage in processing data in this manor is how it handles uncertainties. Each input to the inference process is treated as a distribution rather than an individual point. The inference can further be constrained with previous knowledge, and or physical knowledge about the system using the prior likelyhood term. This is more robust than simple boundaries placed on parameters in other modeling techniques, as it can be extremely flexible in nature. For example if there are disconnected regions where the parameters are disallowed or complex distributions such as a Poisson distribution the routines handles it as easily as simple boundaries. Bayesian inference also provides a mechanism to marginalize over parameters which are uninteresting, complicated to analyze, or unknown and still account for them in parameter determination by modifying the resulting parameter distribution. Finally, Bayesian inference has many implementations which provide a fast and efficient way to explore phase space.

We have shown how the model of a lightcuve given in Gregory (1999) can be modified successfully to account for the systematics of an orbit and determine the pole direction of rotation. Though not shown here, this methodology should be feasible to use on a fairly short time frame. The duration of observations needed to determine the pole direction should be possible to estimate given the expected signal-to-noise ratio, period, and range of pole directions. This will provide a useful tool for observation planning and coordination.

Litva appears to have a fairly standard pole direction for an asteroid of its size. Hanuš et al. (2011) outlines distribution functions for the latitude and longitude of pole directions for many main belt objects. They find the most likely latitude for objects under 30 km to be between 50 and 90 degrees. This agrees quite well with our determined pole direction of approximately 62 degrees. The distribution of longitudes is much more uniform, as one might expect, and thus there is nothing surprising with our determined value of 292 degrees.

We have done a preliminary search based on our methodology for the pole direction of the non tidally locked satellite and determined a period of $5.6815h$, a latitude of 45.34 degrees, and a longitude of 201.1 degrees. We caution that this may or may not be indicative of the true value as the model does not fully take into account the extra degrees of freedom which the satellite has as it orbits the primary body. As such we decline to put formal confidence limits on the pole direction as these limits would not reflect the uncertainty to which the model represents the system it is modeling. To better look for satellite properties we can modify our approach in the following ways. Currently, we have the vectors to the center of Litva in three-dimensional space, i.e. the Litva reference frame. To use the same basic methodology discussed in this paper we would need to have vectors from the center of the satellite to Earth at each observation point. Because the distance to Earth is much greater than the semi-major axis of the satellite's orbit, these lines are expected to be nearly parallel but not exactly. A full model would include parameters for the orbit of the satellite such that the vector offsets from the center of Litva to the center of the satellite could be determined. With the updated vectors, the pole direction of rotation for the satellite could be determined. This would also have the added benefit of providing all of the orbital parameters, as well as the pole direction of the orbit.

The model for the phase delay /advancement can also be adapted to work with an eclipsing model vs that of an alternating sinusoidal function. In this way we could model the eclipsing portion of a satellite for both transit depth and timing to determine the pole direction of the orbital plane as well as orbital parameters.

This work may also benefit from alternative models to that of a step-function. A Fourier series would still be easy to modify to account for the changing phases. This may even prove to be bennificial as a Fourier series is analytic making it easier to marginalize over parameters. A Fourier model would also benefit from the ability of Bayesian inference to differentiate between models, because this would allow for a inference based selection on the number of harmonics to include.

If the preliminary pole direction of the satellite proves to be correct with a more complicated model it would lead to questions such as why the mutual interactions have not damped the two bodies such that their spins are aligned. These questions may provide insight into formation mechanisms which bifurcates pole directions, as it is currently thought that many binaries form from rotational ejection near the equator (Walsh et al., 2008). Further analysis may also reveal if the spin axis and orbital axis are aligned, and what implications that may have for the evolution of the system as a whole.

APPENDIX A: APPENDIX OF FIGURES AND TABLES FOR IRAC 3.6μm ANALYSIS

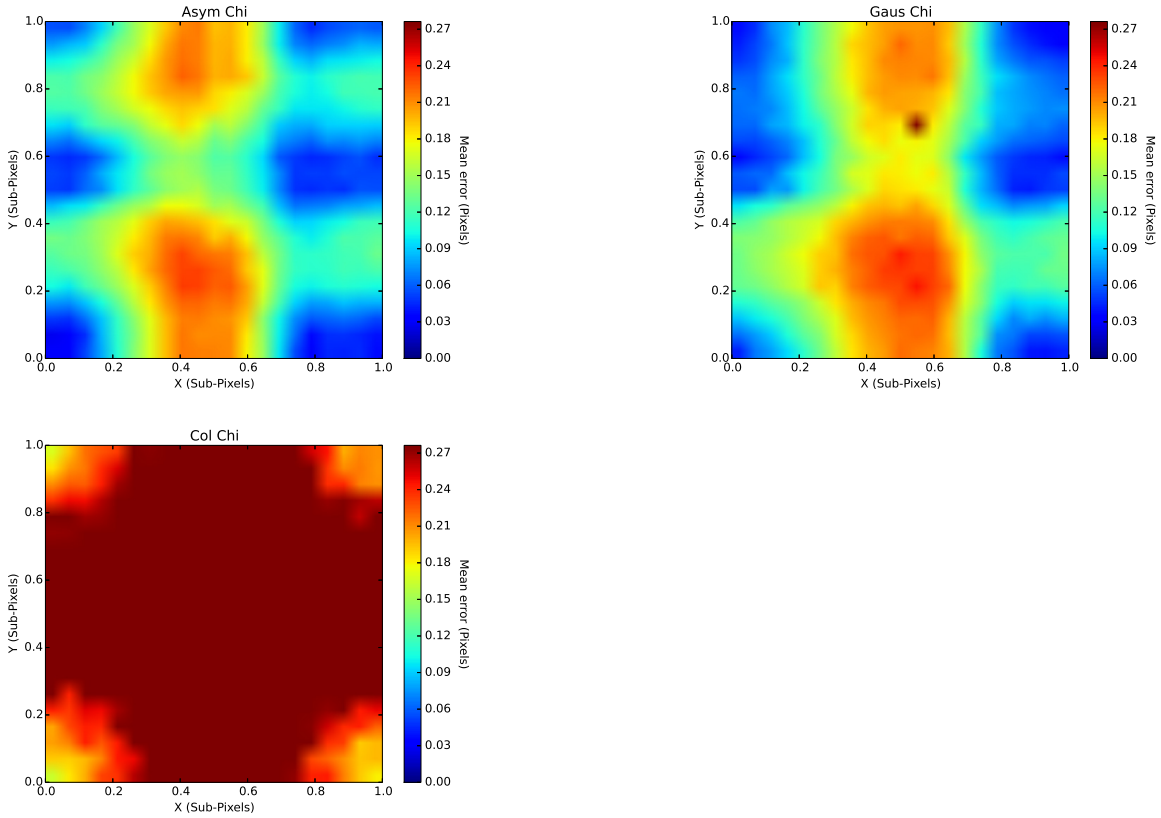

Figure A.1: Goodness of centering in sub-pixel space. Results for Least Asymmetry (top left), Gaussian (top right), and center of light (bottom left) for the 3.6 μm PRF at S/N 10. Blue represents better centering, red worse. The cross pattern arises from a combination of a pixelation effect and the non-uniformity of the PRF.

Table A.1: 3.6 μm PRF Kernel Mean Positional Error (Pixels)

S/N	Asymmetry	Gaussian	Center of Light
1.0	0.6060 (0.0780)	68.943 (107.73)	0.4466 (0.1181)
2.0	0.2030 (0.0400)	0.8195 (4.6259)	0.4355 (0.1150)
3.0	0.1556 (0.0402)	0.2031 (0.1259)	0.4249 (0.1120)
4.0	0.1427 (0.0446)	0.1599 (0.0739)	0.4147 (0.1092)
5.0	0.1369 (0.0475)	0.1476 (0.0603)	0.4050 (0.1064)
6.0	0.1337 (0.0494)	0.1426 (0.0592)	0.3957 (0.1038)
7.0	0.1318 (0.0506)	0.1395 (0.0582)	0.3868 (0.1013)
8.0	0.1305 (0.0516)	0.1390 (0.0583)	0.3783 (0.0989)
9.0	0.1295 (0.0522)	0.1371 (0.0573)	0.3701 (0.0966)
10.0	0.1288 (0.0528)	0.1362 (0.0580)	0.3618 (0.0946)
20.0	0.1264 (0.0549)	0.1334 (0.0607)	0.2972 (0.0768)
30.0	0.1259 (0.0554)	0.1325 (0.0596)	0.2509 (0.0645)
40.0	0.1256 (0.0557)	0.1324 (0.0606)	0.2162 (0.0558)
50.0	0.1255 (0.0558)	0.1326 (0.0607)	0.1894 (0.0494)
60.0	0.1254 (0.0559)	0.1322 (0.0610)	0.1682 (0.0448)
70.0	0.1254 (0.0560)	0.1321 (0.0610)	0.1511 (0.0413)
80.0	0.1253 (0.0560)	0.1320 (0.0610)	0.1371 (0.0387)
90.0	0.1253 (0.0560)	0.1320 (0.0611)	0.1255 (0.0367)
100.0	0.1253 (0.0561)	0.1319 (0.0611)	0.1254 (0.0352)

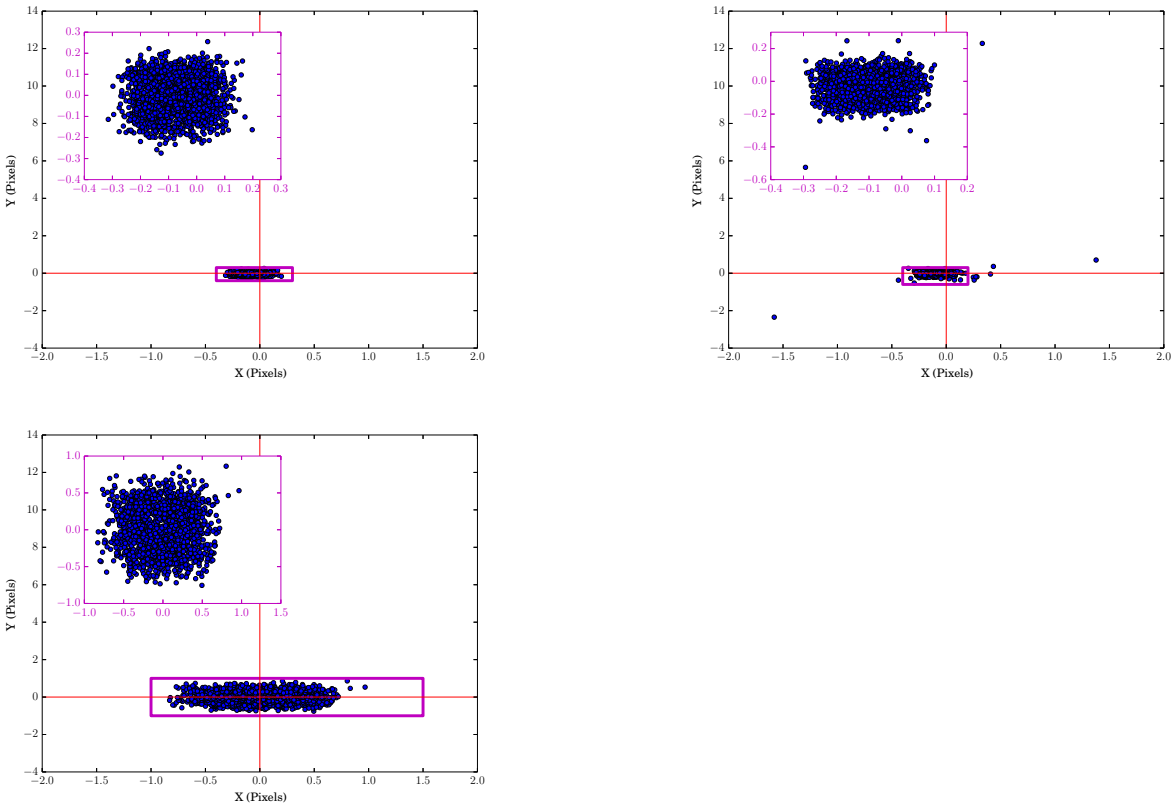

Figure A.2: Routine precision at S/N = 5 on the 3.6 μm PRF- Top: The residuals from asymmetry centering. Middle: The residuals from Gaussian centering. Bottom: The residuals from Center-of-Light centering. Note the axes are the same scale, but the subfigures are a larger view of the magenta square and differ in scale to provide further detail. The red lines indicate the zero point.

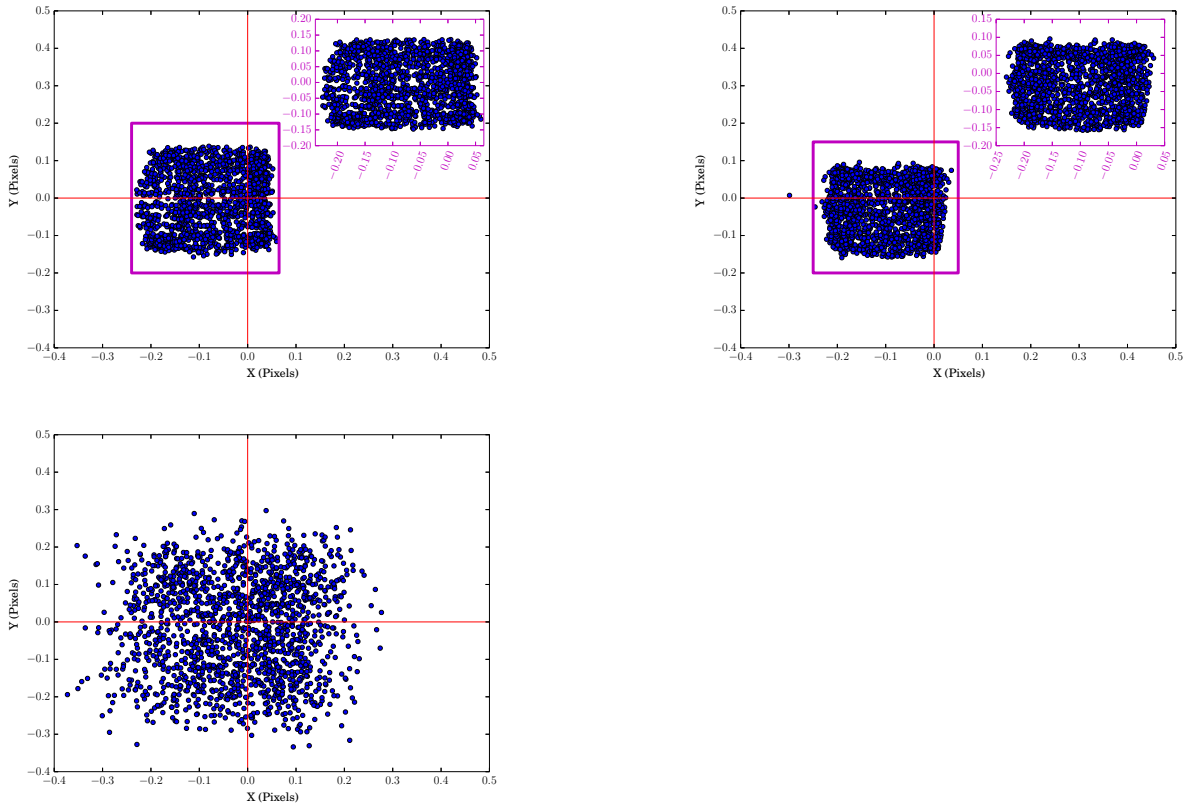

Figure A.3: Routine precision at S/N = 60 on the 3.6 µm PRF- Left: The residuals from least asymmetry centering. Right: The residuals from Gaussian centering. Least asymmetery is more accurate but less precise than Gaussian centering. Note the axes are the same scale, but the subfigures are a larger view of the magenta square and differ in scale to provide further detail. The red lines indicate the zero point.

APPENDIX B: DEFENSE ANNOUNCEMENT

Announcing the Final Examination of Mr. Nate Lust for the degree of Doctor of Physics

Date: November 6, 2014

Time: 3:00 p.m.

Room: Psb 161

Dissertation title: Creation and Application of Routines for Determining Physical Properties of Asteroids and Exoplanets from Low Signal-To-Noise Data-Sets

Astronomy is a data heavy field driven by observations of remote sources reflecting or emitting light. These signals are transient in nature, which makes it very important to fully utilize every observation. This however is often difficult due to the faintness of these observations, often are only slightly above the level of observational noise. We present new or adapted methodologies for dealing with these low signal-to-noise scenarios, along with practical examples including determining exoplanet physical properties, periodicities in asteroids, and the rotational and orbital properties of the multiple asteroid system 2577 Litva.

Outline of Studies:

Major: Planetary Sciences

Educational Career:

B.S., 2007, University of Central Florida

Committee in Charge:

Dr. Daniel Britt

Dr. Yanga Fernandez

Dr. Marianna Pensky

Dr. Alan Harris

Approved for distribution by Daniel Britt, Committee Chair, on October 17, 2014

The public is welcome to attend.

LIST OF REFERENCES

Borucki, W. J., Koch, D., Basri, G., Batalha, N., Brown, T., Caldwell, D., Caldwell, J., Christensen-Dalsgaard, J., Cochran, W. D., DeVore, E., Dunham, E. W., Dupree, A. K., Gautier, T. N., Geary, J. C., Gilliland, R., Gould, A., Howell, S. B., Jenkins, J. M., Kondo, Y., Latham, D. W., Marcy, G. W., Meibom, S., Kjeldsen, H., Lissauer, J. J., Monet, D. G., Morrison, D., Sasselov, D., Tarter, J., Boss, A., Brownlee, D., Owen, T., Buzasi, D., Charbonneau, D., Doyle, L., Fortney, J., Ford, E. B., Holman, M. J., Seager, S., Steffen, J. H., Welsh, W. F., Rowe, J., Anderson, H., Buchhave, L., Ciardi, D., Walkowicz, L., Sherry, W., Horch, E., Isaacson, H., Everett, M. E., Fischer, D., Torres, G., Johnson, J. A., Endl, M., MacQueen, P., Bryson, S. T., Dotson, J., Haas, M., Kolodziejczak, J., Van Cleve, J., Chandrasekaran, H., Twicken, J. D., Quintana, E. V., Clarke, B. D., Allen, C., Li, J., Wu, H., Tenenbaum, P., Verner, E., Bruhweiler, F., Barnes, J., & Prsa, A. 2010, Science, 327, 977

Britt, D. T., Yeomans, D., Housen, K., & Consolmagno, G. 2002, Asteroids III, 485

Campo, C. J., Harrington, J., Hardy, R. A., Stevenson, K. B., Nymeyer, S., Ragozzine, D., Lust, N. B., Anderson, D. R., Collier-Cameron, A., Blecic, J., Britt, C. B. T., Bowman, W. C., Wheatley, P. J., Loredo, T. J., Deming, D., Hebb, L., Hellier, C., Maxted, P. F. L., Pollaco, D., & West, R. G. 2011, ApJ, 727, 125

Chang, S. G., Yu, B., & Vetterli, M. 2000, IEEE TRANSACTIONS ON IMAGE PROCESSING, 9, 1532

Charbonneau, D., Brown, T. M., Burrows, A., & Laughlin, G. 2007, Protostars and Planets V, 701

Crida, A. 2009, ArXiv e-prints

Demory, B.-O., Gillon, M., Barman, T., Bonfils, X., Mayor, M., Mazeh, T., Queloz, D., Udry, S., Bouchy, F., Delfosse, X., Forveille, T., Mallmann, F., Pepe, F., & Perrier, C. 2007, A&A, 475, 1125

Diego, F. 1985, PASP, 97, 1209

Donoho, D. L. & Johnstone, I. M. 1995, Journal of the american statistical association, 90, 1200

Donoho, D. L. & Johnstone, J. M. 1994, Biometrika, 81, 425

Drummond, J. D., Weidenschilling, S. J., Chapman, C. R., & Davis, D. R. 1988, Icarus, 76, 19

Fazio, G. G., Hora, J. L., Allen, L. E., Ashby, M. L. N., Barmby, P., Deutsch, L. K., Huang, J.-S., Kleiner, S., Marengo, M., Megeath, S. T., Melnick, G. J., Pahre, M. A., Patten, B. M., Polizotti, J., Smith, H. A., Taylor, R. S., Wang, Z., Willner, S. P., Hoffmann, W. F., Pipher, J. L., Forrest, W. J., McMurty, C. W., McCreight, C. R., McKelvey, M. E., McMurray, R. E., Koch, D. G., Moseley, S. H., Arendt, R. G., Mentzell, J. E., Marx, C. T., Losch, P., Mayman, P., Eichhorn, W., Krebs, D., Jhabvala, M., Gezari, D. Y., Fixsen, D. J., Flores, J., Shakoorzadeh, K., Jungo, R., Hakun, C., Workman, L., Karpati, G., Kichak, R., Whitley, R., Mann, S., Tollestrup, E. V., Eisenhardt, P., Stern, D., Gorjian, V., Bhattacharya, B., Carey, S., Nelson, B. O., Glaccum, W. J., Lacy, M., Lowrance, P. J., Laine, S., Reach, W. T., Stauffer, J. A., Surace, J. A., Wilson, G., Wright, E. L., Hoffman, A., Domingo, G., & Cohen, M. 2004, ApJS, 154, 10

Foster, G. 1996, AJ, 112, 1709

Gregory, P. C. 1999, ApJ, 520, 361

Haar, A. 1910, 69, 331

Hanuš, J., Ďurech, J., Brož, M., Warner, B. D., Pilcher, F., Stephens, R., Oey, J., Bernasconi, L., Casulli, S., Behrend, R., Polishook, D., Henych, T., Lehký, M., Yoshida, F., & Ito, T. 2011, A&A, 530, A134

Harrington, J., Luszcz, S., Seager, S., Deming, D., & Richardson, L. J. 2007, Nature, 447, 691

Harris, A. W. & Lupishko, D. F. 1989, in Asteroids II, ed. R. P. Binzel, T. Gehrels, & M. S. Matthews, 39–53

Holman, M. J., Fabrycky, D. C., Ragozzine, D., Ford, E. B., Steffen, J. H., Welsh, W. F., Lissauer, J. J., Latham, D. W., Marcy, G. W., Walkowicz, L. M., Batalha, N. M., Jenkins, J. M., Rowe, J. F., Cochran, W. D., Fressin, F., Torres, G., Buchhave, L. A., Sasselov, D. D., Borucki, W. J., Koch, D. G., Basri, G., Brown, T. M., Caldwell, D. A., Charbonneau, D., Dunham, E. W., Gautier, T. N., Geary, J. C., Gilliland, R. L., Haas, M. R., Howell, S. B., Ciardi, D. R., Endl, M., Fischer, D., Fürész, G., Hartman, J. D., Isaacson, H., Johnson, J. A., MacQueen, P. J., Moorhead, A. V., Morehead, R. C., & Orosz, J. A. 2010, Science, 330, 51

Howell, S. B. 1989, PASP, 101, 616

Howell, S. B. 2006, Handbook of CCD Astronomy, 2nd edn. (Cambridge University Press)

IRAC Instrument and Instrument Support Teams. 2013, IRAC Instrument Handbook

Jones, W. B., Njstad, O., & Saff, E. B. 1990, Journal of Computational and Applied Mathematics, 32, 387

Kallrath, J. & Milone, E. F. 2009, Eclipsing Binary Stars: Modeling and Analysis (New York, NY :: Springer-Verlag New York,)

King, I. R. 1971, PASP, 83, 199

Lissauer, J. J., Fabrycky, D. C., Ford, E. B., Borucki, W. J., Fressin, F., Marcy, G. W., Orosz, J. A., Rowe, J. F., Torres, G., Welsh, W. F., Batalha, N. M., Bryson, S. T., Buchhave, L. A., Caldwell, D. A., Carter, J. A., Charbonneau, D., Christiansen, J. L., Cochran, W. D., Desert, J.-M., Dunham, E. W., Fanelli, M. N., Fortney, J. J., Gautier, III, T. N., Geary, J. C., Gilliland, R. L., Haas, M. R., Hall, J. R., Holman, M. J., Koch, D. G., Latham, D. W., Lopez, E., McCauliff, S., Miller, N., Morehead, R. C., Quintana, E. V., Ragozzine, D., Sasselov, D., Short, D. R., & Steffen, J. H. 2011, Nature, 470, 53

Lust, N., Britt, D., & Harris, A. 2011, in EPSC-DPS Joint Meeting 2011, 1512

Madhusudhan, N., Harrington, J., Stevenson, K. B., Nymeyer, S., Campo, C. J., Wheatley, P. J., Deming, D., Blecic, J., Hardy, R. A., Lust, N. B., Anderson, D. R., Collier-Cameron, A., Britt, C. B. T., Bowman, W. C., Hebb, L., Hellier, C., Maxted, P. F. L., Pollacco, D., & West, R. G. 2011, Nature, 469, 64

Mayor, M. & Queloz, D. 1995, Nature, 378, 355

Merline, W. J., Tamblyn, P. M., Warner, B. D., Pravec, P., Tamblyn, J. P., Neyman, C., Conrad, A. R., Owen, W. M., Carry, B., Drummond, J. D., Chapman, C. R., Enke, B. L., Grundy, W. M., Veillet, C., Porter, S. B., Arcidiacono, C., Christou, J. C., Durda, D. D., Harris, A. W., Weaver, H. A., Dumas, C., Terrell, D., & Maley, P. 2013, IAU Circ., 9267, 1

Mighell, K. J., Glaccum, W., & Hoffmann, W. 2008, in Society of Photo-Optical Instrumentation Engineers (SPIE) Conference Series, Vol. 7010, Society of Photo-Optical Instrumentation Engineers (SPIE) Conference Series

Narita, N., Sato, B., Hirano, T., & Tamura, M. 2009, PASJ, 61, L35

Nymeyer, S., Harrington, J., Hardy, R. A., Stevenson, K. B., Campo, C. J., Madhusudhan, N., Collier-Cameron, A., Loredo, T. J., Blecic, J., Bowman, W. C., Britt, C. B. T., Cubillos, P., Hellier, C., Gillon, M., Maxted, P. F. L., Hebb, L., Wheatley, P. J., Pollacco, D., & Anderson, D. R. 2011, ApJ, 742, 35

Pravec, P., Scheirich, P., Vokrouhlický, D., Harris, A. W., Kušnirák, P., Hornoch, K., Pray, D. P., Higgins, D., Galád, A., Világi, J., Gajdoš, Š., Kornoš, L., Oey, J., Husárik, M., Cooney, W. R., Gross, J., Terrell, D., Durkee, R., Pollock, J., Reichart, D. E., Ivarsen, K., Haislip, J., LaCluyze, A., Krugly, Y. N., Gaftonyuk, N., Stephens, R. D., Dyvig, R., Reddy, V., Chiorny, V., Vaduvescu, O., Longa-Peña, P., Tudorica, A., Warner, B. D., Masi, G., Brinsfield, J., Gonçalves, R., Brown, P., Krzeminski, Z., Gerashchenko, O., Shevchenko, V., Molotov, I., & Marchis, F. 2012, Icarus, 218, 125

Pravec, P., Wolf, M., & Šarounová, L. 1998, Icarus, 133, 79

Ryan, H. 1994, CSEG Recorder, 8

Scheirich, P. & Pravec, P. 2009, Icarus, 200, 531

Stellingwerf, R. F. 1978, ApJ, 224, 953

Stevenson, K. B., Harrington, J., Fortney, J. J., Loredo, T. J., Hardy, R. A., Nymeyer, S., Bowman, W. C., Cubillos, P., Bowman, M. O., & Hardin, M. 2012a, ApJ, 754, 136

Stevenson, K. B., Harrington, J., Lust, N. B., Lewis, N. K., Montagnier, G., Moses, J. I., Visscher, C., Blecic, J., Hardy, R. A., Cubillos, P., & Campo, C. J. 2012b, ApJ, 755, 9

Stevenson, K. B., Harrington, J., Nymeyer, S., Madhusudhan, N., Seager, S., Bowman, W. C., Hardy, R. A., Deming, D., Rauscher, E., & Lust, N. B. 2010, Nature, 464, 1161

ter Braak, C. J. F. & Vrugt, J. A. 2008, Statistics and Computing, 18, 435

Walsh, K. J., Richardson, D. C., & Michel, P. 2008, Nature, 454, 188

Warner, B. D., Harris, A. W., & Pravec, P. 2009a, Icarus, 202, 134

Warner, B. D., Pravec, P., Harris, A. W., Higgins, D., Bembrick, C., Brinsfield, J. W., Pray, D. P., Pollock, J., Reichart, D., Ivarsen, K., Haislip, J., Lacluyze, A., & Galad, A. 2009b, Minor Planet Bulletin, 36, 165

Werner, M. W., Roellig, T. L., Low, F. J., Rieke, G. H., Rieke, M., Hoffmann, W. F., Young, E., Houck, J. R., Brandl, B., Fazio, G. G., Hora, J. L., Gehrz, R. D., Helou, G., Soifer, B. T., Stauffer, J., Keene, J., Eisenhardt, P., Gallagher, D., Gautier, T. N., Irace, W., Lawrence, C. R., Simmons, L., Van Cleve, J. E., Jura, M., Wright, E. L., & Cruikshank, D. P. 2004, ApJS, 154, 1

Winn, J. N. 2009, in IAU Symposium, Vol. 253, IAU Symposium, ed. F. Pont, D. Sasselov, & M. J. Holman, 99–109

99